In Press: *Journal of Clinical Investigation*

An allosteric inhibitor of sirtuin 2 deacetylase activity exhibits broad-spectrum antiviral activity

Kathryn L. Roche,[1] Stacy Remiszewski,[1] Matthew J. Todd,[1] John L. Kulp III,[1] Liudi Tang,[1] Alison V. Welsh[1], Ashley P. Barry,[2] Chandrav De,[3] William W. Reiley,[4] Angela Wahl,[3] J. Victor Garcia-Martinez,[3] Micah A. Luftig,[2] Thomas Shenk,[1,5] James R. Tonra,[1] Eain A. Murphy,[1,6] and Lillian W. Chiang,[1]

[1]Evrys Bio, LLC, Pennsylvania Biotechnology Center, Doylestown, Pennsylvania 18902. [2]Department of Molecular Genetics and Microbiology, Duke Center for Virology, Duke University School of Medicine, Durham, North Carolina 27710. [3]International Center for the Advancement of Translational Science, Division of Infectious Diseases, Center for AIDS Research, University of North Carolina, School of Medicine, Chapel Hill, North Carolina 27599. [4]TICRO Bioservices, Trudeau Institute, Saranac Lake, New York 12983. [5]Department of Molecular Biology, Princeton University, Princeton, New Jersey 08540. [6]Microbiology and Immunology Department, SUNY Upstate Medical University, Syracuse, New York 13210.

Corresponding author: Lillian W. Chiang, Ph.D., Evrys Bio, LLC, 3805 Old Easton Road, Doylestown, PA 18902; phone, 267-370-5436; e-mail, lillian@evrysbio.com

Conflict of Interest statement: KLR, SR, MJT, JLK, LT, AVW, JRT, EAM and LWC are or have been employees of Evrys Bio, receiving income from the company and owning company stock. TS is a founder of Evrys Bio and owns company stock, and MAL is a member of the Evrys Bio Scientific Advisory Board and owns company options.

Abstract

Most drugs used to treat viral disease target a virus-coded product. They inhibit a single virus or virus family and the pathogen can readily evolve resistance. Host-targeted antivirals can overcome these limitations. The broad-spectrum activity achieved by host targeting can be especially useful in combating emerging viruses and for treatment of diseases caused by multiple viral pathogens, such as opportunistic agents in immunosuppressed patients. We have developed a family of compounds that modulate sirtuin 2, an NAD^+-dependent deacylase, and now report the properties of a member of that family, FLS-359. Biochemical and X-ray structural studies show that the drug binds to sirtuin 2 and allosterically inhibits its deacetylase activity. FLS-359 inhibits the growth of RNA and DNA viruses, including members of the coronavirus, orthomyxovirus, flavivirus, hepadnavirus and herpesvirus families. FLS-359 acts at multiple levels to antagonize cytomegalovirus replication in fibroblasts, causing modest reductions in viral RNAs and DNA, together with a much greater reduction in infectious progeny, and it exhibits antiviral activity in humanized mouse models of infection. Our results highlight the potential of sirtuin 2 inhibitors as broad-spectrum antivirals and set the stage for further understanding of how host epigenetic mechanisms impact the growth and spread of viral pathogens.

Graphical Abstract

Substrate-selective
Sirtuin 2 Inhibitor

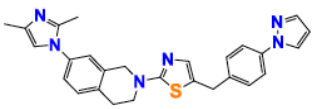

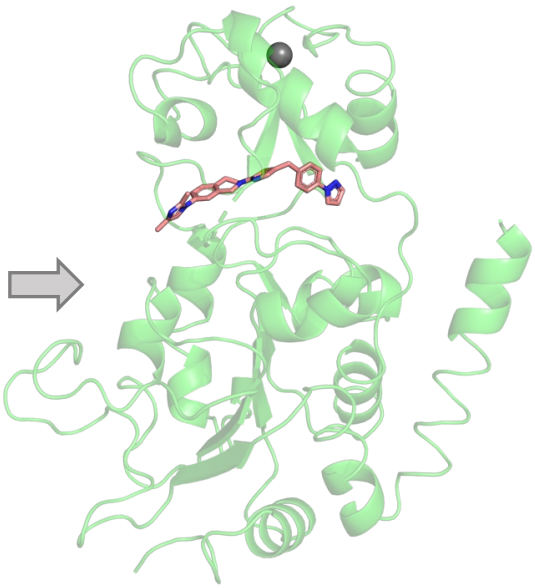

Host-coded Target
Engagement

Broad-spectrum
Antiviral Activity

Herpesviridae
Hepadnaviridae
Coronaviridae
Orthomyxoviridae
Flaviviridae
others…

Introduction

Direct-acting antivirals (DAAs) target virus-coded products and are a highly successful therapeutic paradigm. The sofosbuvir/velpatasvir combination, which inhibits the hepatitis C virus polymerase complex, is a case in point. It cures a high portion of patients with chronic hepatitis C (1). However, DAAs suffer from two principal limitations. First, viruses develop resistance, as is well documented for influenza M2 ion channel and neuraminidase inhibitors (2). Second, although there are exceptions (3), DAAs generally target only one virus or virus family.

In contrast to DAAs, host-targeted antivirals (HTAs) inhibit a host product that supports viral replication or enhance the activity of a defensive network. With no selective pressure for the accumulation of mutations in host cell antiviral targets, viral resistance should not develop. Further, since different viruses use overlapping cellular pathways and factors to support their replication (4) and antiviral defense systems often target these common pathways, HTAs can exhibit broad-spectrum activity (5). Thus, HTAs have potential to treat categories of viral disease where the causative agents span multiple virus families. Importantly, broad-spectrum HTAs have potential to provide a rapid therapeutic solution at the onset of a pandemic, reducing the time between novel virus identification and pharmacological intervention (6, 7). Beyond this periodic need, HTAs can treat patients at risk for infection with viruses of different families, such as transplant patients who are at elevated risk for herpesvirus, paramyxovirus, polyomavirus, hepadnavirus and coronavirus infections during immunosuppressive therapy (8, 9).

One intriguing network of targets for the development of HTAs are the proteins that create and read the cellular acetylome. Lysine N-ε-acetylations are found on thousands of proteins (10). Histone acetyltransferases (HATs) transfer an acetyl group from acetyl-coenzyme A to a target lysine, bromodomain-containing proteins read these modified lysine residues to

regulate diverse cellular processes, and histone deacetylases (HDACs) remove the marks. The dynamic interplay between HATs and HDACs specifies the acetylome, which impacts chromatin structure and transcriptional activity, protein-protein interactions, protein localization and metabolic processes (11, 12).

Not surprisingly, given their broad impact on cellular processes, lysine N-ε-acetylations modulate factors critical for viral replication. For example, transcription of the HIV genome is influenced by histone acetylation, the viral integrase and transactivator of transcription (Tat) proteins are regulated by acetylation, and HIV latency is modulated by drugs that inhibit deacetylation (13). Likewise, influenza A proteins are regulated by acetylation (14), and human cytomegalovirus (HCMV) infection profoundly impacts the cellular and viral acetylomes (15). In addition to supporting viral processes, lysine acetylation also impacts cellular antiviral defense systems. For example, the location of the DNA sensor protein, gamma-interferon-inducible protein 16 (IFI16), is controlled by acetylation (16), and the activity of nuclear factor kappaB (NF-κB), which regulates numerous elements of immune responses, is modulated via acetylations within its p65 subunit (17).

The inhibition of deacetylation has been explored as an antiviral mechanism. HDACs form two major families: Zn^{++}-dependent HDACs and NAD^{+}-dependent HDACs, also termed sirtuins (SIRTs). The seven SIRTs (SIRT1-7) (18) transfer an acyl group from an acylated lysine of a protein substrate to the ADP-ribose moiety of NAD^{+}, deacylating the protein and producing nicotinamide (NAM) plus 2'-O-acyl-ADP ribose (19). De-acetylation is most commonly studied, but SIRTs also remove longer-chain acyl-groups (20). The NAD^{+} requirement ties SIRT activity to the metabolic state of cells, and infection significantly disrupts cellular metabolism (21, 22). The human SIRTs are localized to distinct cellular compartments (23), and knockdown of each

human SIRT, as well as the *E. coli* SIRT, CobB, modulates the growth of multiple viruses (24), underscoring their evolutionarily conserved roles in the control of viral replication. The dual SIRT1/2 inhibitors, tenovin-1 and sirtinol, inhibit the growth of both RNA and DNA viruses (25, 26); and the SIRT2-selective inhibitor, AGK2 (27), antagonizes the replication of hepatitis B virus (28, 29). SIRT2 knockout mice are healthy and immunocompetent (30, 31), arguing that selective SIRT2 inhibitors are likely to be well tolerated as antiviral therapeutics.

Here we explore the utility of small molecules targeting SIRT2 as broad-spectrum antivirals with potential to treat opportunistic infections. We demonstrate that the compound, FLS-359, binds to SIRT2 and allosterically inhibits its deacetylase activity. Broad-spectrum antiviral activity of the drug is evident across multiple DNA and RNA virus families, including the herpesviruses, human cytomegalovirus (HCMV) and Epstein-Barr virus (EBV), which are of particular concern in immunosuppressed patients (32–36). The drug reduces the accumulation of HCMV RNAs and DNA, substantially decreasing virus spread and infectious yield in human fibroblasts. FLS-359 also reduced virus production in two humanized mouse models of HCMV infection. These results highlight SIRT2 as a host target, and support further development of drugs targeting SIRT2 as broad-spectrum antivirals.

Results

FLS-359 binds SIRT2, selectively reducing deacetylase activity. Starting with a hit from a small molecule screen designed to identify compounds that altered SIRT2 activity in vitro, we developed a portfolio of molecules targeting SIRT2 using anti-HCMV activity as a primary criterion in our lead optimization campaign. FLS-359, 7-(2,4-dimethyl-1H-imidazol-1-yl)-2-(5-{[4-(1H-pyrazol-1-yl)phenyl]methyl}-1,3-thiazol-2-yl)-1,2,3,4-tetrahydroisoquinoline (Figure 1A), is a representative lead.

An in vitro thermal shift assay (37) was used to test for FLS-359-SIRT2 binding by quantifying the compound-dependent increase in protein thermal stability (Figure 1B). SIRT2 underwent thermal denaturation with a T_m ~ 48ºC. FLS-359 increased the T_m by 1.4ºC (6.25 μM) or 2.0ºC (12.5 μM), demonstrating that the drug engages and stabilizes the purified protein.

The effect of FLS-359 on deacetylation of a peptide containing a histone H3 acetylation site (Ac-H_3K_9WW) was assayed in vitro, using mass spectrometry to quantify deacetylated peptide. The concentration for half-maximal inhibition (IC_{50}) in this assay was ~3 μM for SIRT2 and >100 μM for SIRT1 and SIRT3 (Figure 1C). When the NAD^+ concentration was increased from 50 to 100, 200, and 500 μM, more deacetylated product was generated, but the IC_{50} remained essentially the same (Figure 1D, E). The IC_{50} was ~3 μM for all NAD^+ concentrations when the peptide was used at 5 μM. The IC_{50} was ~7 μM for all NAD^+ concentrations at 50 μM peptide. Therefore, FLS-359 is not competitive with NAD^+. When the peptide concentration was increased from 5 μM (1x K_m, Figure 1D) to 50 μM peptide (10x K_m, Figure 1E), the IC_{50} increased from ~3 μM to ~7 μM or ~2-fold. If FLS-359 binding was fully competitive with the peptide, an ~10-fold increase in IC_{50} would be expected. In addition, saturating compound decreased SIRT2 activity to a lower but residual value. Both of these observations are consistent

with partial inhibition, seen with other SIRT2 inhibitors, e.g., AGK2 (38) and MIND4 (39). Since SIRT2 is important to cellular metabolic homeostasis, the observed partial inhibition may prove to be a positive attribute that supports cell viability in uninfected cells while providing an antiviral effect in infected cells.

SIRT2 has deacylation activities in addition to deacetylation (20, 40), including demyristoylation, and several SIRT2 inhibitors are acyl-group selective, blocking deacetylation but not demyristoylation (41–44). When tested for inhibition of demyristoylation using the same peptide backbone (Myr-H_3K_9WW) used to assay deacetylation (Ac-H_3K_9WW), neither FLS-359 nor tool compounds (AGK2 and SirReal2) showed activity (Fig. 1F, G). Thus, FLS-359 is substrate selective, inhibiting deacetylation but not demyristoylation.

FLS-359 induces known activities of SIRT2 modulators within cultured cells. SIRT2 deacetylates α-tubulin K40 (45); and, as expected, treatment of cultured HepG2 hepatocellular carcinoma cells with FLS-359 for 24h increased the level of acetylated α-tubulin in HepG2 cells by a factor of ~3 (Supplemental Figure 1A). SIRT2 knockdown or inhibition induces degradation of c-Myc protein in tumor cells by inducing its ubiquitination (46, 47), and treatment with FLS-359 for 72h dramatically reduced the level of the oncoprotein in MDA-MB-231 breast adenocarcinoma cells (Supplemental Figure 1B). Of note, c-Myc levels were not changed by treatment of MRC-5 human diploid fibroblasts with the drug (Supplemental Figure 1C). Thus, treatment with FLS-359 induces known consequences of SIRT2 inhibition in tumor cells.

X-ray structure confirms FLS-359 engagement of SIRT2. X-ray crystallographic structures have been determined for human SIRT1, 2, 3, 5 and 6 (48). The structures consist of two domains: an upper Zn^{++}-binding domain and a lower catalytic domain with a Rossman fold (49, 50). The two domains behave as a clamshell, accommodating varying acyl-Lys

161 modifications within a flexible pocket between the two clamshell domains. This area is above the
162 C-pocket of the NAD^+-binding site and is termed the extended C (EC) pocket (50). SIRT1, 2,
163 and 3 are ~70-80% conserved around the NAD^+ and nearby EC pockets, where natural and
164 synthetic small molecule ligands that affect activity have been resolved (48, 50).
165 We produced crystals of FLS-359 bound to SIRT2 that diffracted to 1.8 Å resolution and
166 determined the structure of the complex (Supplemental Table 1). FLS-359 sits in the SIRT2 EC
167 pocket (Figure 2A and B). In comparison to the unliganded SIRT2 apo structure [(51); PDB ID
168 3ZGO], the clamshell has opened and an ordered alpha helix has shifted to an unstructured loop
169 (residues 294-304); in addition, a loop over the drug binding site is rearranged (Supplemental
170 Figure 2). The two substrates, acetyl-lys (PDB ID 4RMI) and NAD^+ (PDB ID 4RMG), are
171 computationally superimposed in Figure 2B. NAD^+ binding is not predicted to be affected by
172 FLS-359 binding. In contrast, the FLS-359 dimethylimidazole moiety resides in the same
173 location as the peptidic acetyl-group, but computational superpositioning predicts that the pocket
174 can accommodate both FLS-359 and the peptide. The binding interactions of FLS-359 with
175 SIRT2 include π-π interactions with residues F119, F190, and Y139 (Figure 2C). Water residue
176 566 bridges FLS-359 and SIRT2 with one hydrogen bond to the thiazole of FLS-359 and another
177 hydrogen bond to the backbone carbonyl of residue F96. A multi-body water network in the
178 peptide channel connects, via a hydrogen bond network, the dimethyl imidazole of FLS-359 to
179 E116 through water residue 371 and to the side chain of R97 through water residues 371, 165,
180 and 652. These water mediated hydrogen bonds could be key interactions that drive binding
181 affinity to SIRT2 in the hydrophobic EC site.
182 The FLS-359/SIRT2 structure was used to probe the substrate-selective activity of the
183 drug. Flexible protein docking confirmed that acetyl-lys (PDB ID 4RMI) and FLS-359 can

simultaneously bind within the SIRT2 EC pocket (Supplemental Figure 3A), whereas thiomyristoylated peptides (PDB IDs 4R8M and 4X3P) are predicted to compete for binding with the drug (Supplemental Figure 3B, C). Thus, myristolylated peptides have potential to exclude FLS-359 binding, providing an explanation for the drug's substrate-selective activity.

In sum, enzyme thermal denaturation and kinetics studies (Figure 1), as well as co-crystal structure determination (Figure 2), argue that FLS-359 binds selectively to SIRT2 and induces an allosteric rearrangement of the active site, reducing the rate of deacetylation. It is a substrate-selective inhibitor, blocking deacetylation but not demyristoylation.

FLS-359 exhibits broad-spectrum antiviral activity. FLS-359 was tested for activity against multiple RNA and DNA viruses in cultured cells. The drug inhibited the growth of each pathogen shown (Table 1). The IC_{50} varied across the viruses, but the differences must be interpreted with caution, because the assays were performed at different research sites and used a variety of host cells. Nevertheless, in multiple cases, the antiviral IC_{50}s were in the range of current standards of care, with acceptable half-maximal cytotoxic concentrations (CC_{50}s). Most assays were performed in primary cells or diploid cell lines, because SIRT2 inhibition is antiproliferative or cytotoxic to many tumor cell lines (47, 52).

Given the importance of EBV and HCMV as adventitious agents in immunosuppressed patients, (32–36) the effects of FLS-359 were examined in greater detail for these viruses. A broad-spectrum antiviral able to treat both infections has substantial potential utility.

FLS-359 inhibits EBV lytic reactivation and/or replication. The Akata Burkitt lymphoma cell line is permissive for EBV lytic reactivation through activation of the B-cell receptor (53). As expected, 24h following receptor engagement with anti-IgG, 30% of Akata cells induced surface expression of the late EBV gene, gp350, which serves as a proxy for cells that are

replicating viral DNA and forming new virions (Figure 3A). In the presence of the viral DNA replication inhibitor, phosphono-acetic acid (PAA), gp350+ cells were reduced to ~11% (Figure 3A). FLS-359 treatment led to a dose-dependent decrease in gp350+ cells with 10 μM drug inhibiting EBV reactivation at a similar level to PAA (Figure 3A, B). The FLS-359 CC_{50} for Akata cells was >100 μM (Table 1), so the inhibition of gp350 accumulation was not due to drug-induced cytotoxicity. The drug also inhibited the accumulation of a viral immediate-early (BZLF1), early (BMRF1) and late (BLLF1) mRNA (Figure 3C-E). We conclude that FLS-359 markedly reduces EBV lytic activation in Akata cells.

FLS-359 inhibits HCMV spread in diploid fibroblasts. The antiviral activity of a drug is generally measured by assaying its effect on the production of infectious viral progeny. However, many viruses spread via two modes, either by release of a particle that eventually infects a new cell or by direct cell-to-cell transfer (54, 55). HCMV can move by either mechanism, and subviral particles can move from cell to cell, allowing the virus to spread without producing infectious particles (56). To capture the effect of drugs on HCMV movement and amplification by either mechanism, we employed a spread assay. It uses a clinical isolate, TB40/E-mCherry-UL99eGFP (57), containing two reporters to monitor infection of MRC-5 fibroblasts: mCherry controlled by the SV40 early promoter, expressed with immediate-early kinetics, and eGFP fused to the viral UL99 coding region, expressed with late kinetics. The assay protocol is simple: infect confluent fibroblasts at a low input multiplicity (0.01 IU/cell), add drug immediately following infection, and quantify the area expressing fluorescent markers after 7 days (Figure 4A). The extended, 7-day assay reflects the fact that HCMV replicates and spreads slowly, with a single cycle of growth extending over 72-96h in MRC-5 cells. FLS-359 was well tolerated by confluent MRC-5 cells over 7 days, when assayed by counting nuclei (Figure 4B) or

neutral red uptake (Figure 4C); and it was also tolerated by dividing MRC-5 cells over 6 days (Supplemental Figure 4). FLS-359 reduced the total infected cell area marked by mCherry expression in confluent fibroblasts (Figure 4D and E). Reduced mCherry expression was also evident when monitored by Western blot assay (Supplemental Figure 5), mimicking expression of the viral immediate-early viral protein, IE1. This assay indicates that FLS-359 inhibits HCMV spread with an $IC_{50} = 0.466 \pm 0.203$ μM (Figure 4F). Control anti-HCMV drugs acting at different steps in the viral replication cycle, ganciclovir and letermovir, exhibited IC_{50}s of 1.86 and 0.003 μM repectively, consistent with literature reports (58, 59). The potencies measured using the spread assay were similar to potencies determined by $TCID_{50}$ assay of virus in the medium (Figure 4G).

Although letermovir efficiently reduced extracellular infectivity (Figure 4G), it reduced infected cell area to a lesser extent (4-fold) than ganciclovir (33-fold), or FLS-359 (> 100-fold) (Figure 4F). Part of this effect could result from a failure of letermovir to eliminate originally infected cells. However, letermovir blocks at a late point in the viral replication cycle, inhibiting the virus-coded terminase subunit pUL56 (60, 61), which cleaves a unit genome of viral DNA as it enters the capsid. Earlier work has shown that HCMV capsids can spread directly from cell-to-cell (56), and a portion of the residual spread observed with letermovir might result from movement of partially assembled DNA-capsid complexes.

To test whether inhibition of HCMV is a general feature of SIRT2 inhibitors, we assayed tool compounds: AGK2 (27), AK-7 (62), SirReal2 (50), MIND-4 (39) and TM (47) (Table 2, Supplemental Figure 6). Although they were less potent than FLS-359, all of the SIRT2 inhibitors reduced HCMV spread. Since the inhibitors have very different structures (Table 2),

this result argues that they all inhibit HCMV at least in part through targeted modulation of SIRT2.

Having demonstrated the broad-spectrum antiviral attributes of FLS-359, including anti-herpesvirus activity, we focused on the drug's parameters as an anti-HCMV agent.

FLS-359 reduces HCMV spread when administered after an infection has been initiated. To model the ability of FLS-359 to control an established infection in comparison to current standards of care, MRC-5 fibroblasts were infected (0.1 IU/cell) and treated with drug either immediately or after a delay of 1-4 days (Figure 5A). Drug treatment was maintained for 5 days, and then the effect of the delay was assayed by monitoring viral spread. FLS-359, ganciclovir and letermovir each exhibited antiviral activity when administered after a delay (Figure 5B) without inducing toxicity at effective doses (Figure 5C). Indeed, the antiviral IC_{50}s remained essentially unchanged as the addition of drug was delayed over increasing intervals (Figure 5D). The maximal fold reductions for infected cell areas with drug treatment achieved in this experiment (Figure 5D) were less than in the earlier experiment (Figure 4F), because cells were infected at a 10-fold higher input multiplicity and then assayed after a 2-day shorter viral growth period. Still, at each delayed time of drug addition, a greater maximal fold reduction of infected cell area was achieved by treatment with FLS-359, compared to ganciclovir or letermovir. Thus, FLS-359 maintains its antiviral potency when administered at 4 days after the initiation of infection, while demonstrating superior control of viral spread compared to standards of care.

FLS-359 induces an antiviral state that persists after the drug is withdrawn. Long-lasting consequences of SIRT2 modulation could result from a long intracellular half-life of the compound or from modifications to the cellular acylome. Accordingly, we performed a treat-release experiment in which MRC-5 cells were infected (0.5 IU/cell) for 96h in the presence of

drug, drug was removed and virus growth was monitored by $TCID_{50}$ assay of culture medium for an additional 96h (Figure 6A). Cells treated with vehicle (DMSO) lacking drug served as a control, and continued to produce virus throughout the time course (Figure 6B). Release of the letermovir-induced block generated detectable progeny at 24h, the first time monitored after release, with a resumption of growth kinetics similar to that in DMSO-treated cultures; release of the ganciclovir block generated detectable progeny at 48h; and release from the FLS-359 block did not generate progeny over the full 96h period that was monitored. Minimal cellular toxicity was evident in FLS-359 treated cultures at 96h after removal of the drug (Figure 6C, D), arguing against a non-specific toxic effect.

The long-term efficacy of FLS-359 after washout in the treat-release protocol with only a portion of cells infected suggested that the drug might protect uninfected cells from subsequent infection. This possibility was tested in a treat-release-infect experiment where MRC-5 cells were treated with drug for 24h, drug was removed for 72h, and then cells were infected (0.5 IU/cell) and infected cell area was measured at 72 hpi (Supplemental Figure 7A). Whereas treatment with FLS-359 followed by a 72h washout inhibited viral spread (IC_{50} = 4.8 μM), ganciclovir had no activity in the same assay (Supplemental Figure 7B). In a control experiment, both drugs were active when readministered at the time of infection (Supplemental Figure 7C). This indicates that FLS-359 alters the susceptibility of cells to infection, but does not speak to the mechanism.

The long-term efficacy of FLS-359 could result form a prolonged intracellular half life. Therefore, its half life was monitored in uninfected MRC-5 cells by treating with drug for 24h, removing medium with drug and washing cells, and then quantifying drug levels by mass spectrometry (Supplemental Figure 8A). A reduced but significant level of FLS-359 (~5 μM)

298 was detected in cells and supernatant at 72h after drug removal, whereas the control drug,
299 letermovir, was effectively removed from supernatant and cells by washing (Supplemental
300 Figure 8B, C). As a control, FLS-359 was added to medium in cell culture dishes without cells,
301 and it was efficiently removed by washing (Supplemental Figure 8D, E), ruling out the
302 possibility that the drug was simply sticking to the plastic dishes. FLS-359 induces a relatively
303 long lasting pharmacodynamic effect in both infected and uninfected cells that inhibits HCMV
304 replication, at least in part due to an extended intracellular half life.

305 *FLS-359 inhibits the accumulation of intracellular HCMV RNAs and DNA and reduces*
306 *the infectivity of virus progeny.* To evaluate the site in the viral replication cycle that is sensitive
307 to SIRT2 inhibition, we monitored the accumulation of representative immediate-early, early and
308 late HCMV protein-coding RNAs. MRC-5 cells were infected (3 IU/cell), cells were harvested
309 and RNAs were quantified by qRT-PCR assay at 72 hpi (Figure 7A). All of the viral protein-
310 coding RNAs tested were reduced by the SIRT2 inhibitor, and in most cases, the reduction was
311 dose dependent (Figure 7B). The immediate-early UL123 (IE1) and UL122 (IE2) RNAs encode
312 master regulators that modulate expression of the other viral genes (63, 64), so it is possible that
313 an inhibitory event reducing their levels propagates to reduce accumulation of the remaining
314 genes that were assayed.

315 FLS-359 also reduced the level of HCMV-coded long non-coding RNAs (lncRNAs),
316 including RNA4.9, which crosses the viral origin of DNA replication (oriLyt), as well as the
317 UL57 and UL69 protein-coding RNAs that flank the oriLyt (Figure 7C). Reduced accumulation
318 of RNA4.9 restricts HCMV DNA accumulation (65). In addition, UL44, 54 and 57 - all of which
319 are reduced by drug treatment - encode products that function directly in viral DNA replication
320 (66). UL44 and 54 encode subunits of the viral DNA polymerase and UL57 encodes a single-

stranded DNA-binding protein. Not surprisingly, then, intracellular viral DNA accumulation was compromised by treatment with FLS-359 for 72h (Figure 8A) in a dose-dependent manner (Figure 8B). As expected, ganciclovir, a 2'-deoxyguanosine analog, also inhibited intracellular viral DNA accumulation, when tested using doses equivalent to its IC_{50} and IC_{90}. In contrast, letermovir, which acts at a post-replication step, did not have a significant effect on DNA accumulation. FLS-359 reduced the production of infectious virus to below the limit of quantification, whereas ganciclovir and letermovir reduced virus yield to a more limited extent, as expected for the doses tested (Figure 8C). To further evaluate the effect of FLS-359 on virus production, cells were infected and drug treatment was initiated at 2 hpi, maintained until 96 hpi and then the infectivity of progeny virus particles was evaluated (Figure 8D). As seen for the 72h treatment (Figure 8C), virus infectivity was dramatically reduced by the 96h drug treatment (Figure 8E). At 1.0 μM FLS-359, the particle-to-infectious unit was reduced by a factor of 14.5, while 2.5 or 5.0 μM drug reduced infectivity > 1690-fold. In a control experiment, incubation of a virus stock with FLS-359 (1 or 5 μM) for 96 h at 37°C had no significant effect on infectivity (Figure 8F), ruling out the possibility that the drug inactivates virions. Thus, FLS-359 reduces the accumulation of intracellular viral nucleic acids, the production of extracellular virus particles and the infectivity of the virus particles that are generated.

FLS-359 inhibits HCMV infection in two humanized mouse models. FLS-359 pharmacokinetics were assessed in female Balb/c mice (Supplemental Table 2). After a single 50 mg/kg oral (p.o.) dose, the drug exhibited an ~6h plasma $t_{1/2}$, achieving maximal plasma concentrations (C_{max}) of 89 μM, substantially exceeding the in vitro IC_{50}s. The relatively long $t_{1/2}$ and high C_{max} resulted in good exposure, with an AUC of 713 μM•h/mL. FLS-359 was also administered to NOD/Shi-scid/IL-2Rγ^{null} (NOG) mice at 50 mg/kg p.o. twice per day (b.i.d.) for

14 days. No weight loss and no adverse clinical signs were observed, indicating FLS-359 is well tolerated at this dose and schedule.

The inhibitory activity of FLS-359 was tested in two humanized models of HCMV infection. The first (59, 67) used TB40/E virus-infected MRC-5 fibroblasts (0.05 IU/cell), seeded into a collagen matrix (Gelfoam) and then implanted subcutaneously ($1x10^6$ infected cells) into immunodeficient mice. FLS-359 (50 mg/kg, p.o., b.i.d.), valganciclovir (50 mg/kg, p.o., q.d.) or diluent were administered beginning immediately after implantation. Implants were recovered on day 11 after infection, and $TCID_{50}$ assays revealed that both drugs significantly reduced virus production (Figure 9A). We also tested the efficacy of FLS-359 in humanized lung-only mice (LoM), generated by subcutaneous implantation of human lung tissue into immune deficient mice (68). In this model, the human lung tissue expands to form a highly vascularized palpable implant that contains human fibroblast, epithelial, endothelial, and mesenchymal cells which form lung-like structures that support HCMV replication and in vivo efficacy testing of anti-viral agents (68, 69). Administration of FLS-359 (50 mg/kg, p.o., b.i.d.), ganciclovir (100 mg/kg, i.p., q.d.) or diluent was initiated 2 h prior to infection of human lung implants by direct inoculation of TB40/E virus (4.25×10^5 IU/implant). Drug treatments were continued until the lung implants were removed on day 17 after infection and virus was quantified by $TCID_{50}$ assay. Both drugs again significantly reduced the production of infectious HCMV progeny (Figure 9B), confirming in vivo activity of the SIRT2-targeted drug.

Discussion

FLS-359 bound SIRT2 between its Zn^{++}-binding domain and the catalytic Rossman fold domain (Figure 2), in the EC pocket where other small molecule ligands have been localized (50). A thermal shift assay (Figure 1B), and inhibition of deacetylase activity (Figure 1C, D) confirmed drug binding. FLS-359 decreases SIRT2 deacetylase activity, but SIRT2 remains partially active when fully occupied by drug, as seen with other tool compounds, e.g. AGK2 (38) and MIND4 (39), possibly because FLS-359 sits in the EC pocket, but the acetyl-peptide substrate can still bind and undergo catalysis, albeit at a reduced rate. This explanation is consistent with the small decrease in SIRT2 activity at 10x K_m concentration of acetyl-substrate peptide (Figure 1D), and argues that the drug is an allosteric modulator. The movement in the FLS-359/SIRT2 crystal structure (Supplemental Figure 2) when compared to apo-structure [(51); PDB ID 3ZGO], is consistent with this allosteric binding mechanism.

FLS-359 binds and modulates SIRT2 in vitro (Figure 1) and within cells (Supplemental Figure 1), but does FLS-359 antiviral activity result from SIRT2 modulation? Although we have documented robust anti-HCMV activity for FLS-359 (Figure 4), it has been reported that knockdown of SIRT2 increases the yield of HCMV by a factor of ~4 at 96 hpi (24). This apparent contradiction likely results from the different functional consequences of a knockout/knockdown that ablates all SIRT2 activities, as compared to SIRT2-modulating drugs that exhibit substrate selectivity (41–44). SIRT2 removes a variety of long-chain acyl groups in addition to acetyl groups in biochemical assays (19, 20), and FLS-359 blocks SIRT2 deacetylation but not demyristoylation (Figure 1 F, G). Modeling predicts that SIRT2 can accommodate both an acetyl group and FLS-359, whereas the binding of a myristoyl group excludes FLS-359 (Supplemental Figure 3). As a consequence, FLS-359 can modulate SIRT2

deacetylation, but cannot inhibit demyristoylation activity; and it is possible that additional acylations escape inhibition by the drug. Substrate-selective drugs have been described for a variety of enzymes (43), and knockdown/knockout experiments cannot reliably predict the physiological consequences of their activities. One approach that addresses this experimental conundrum is to test the activity of multiple, different drugs that modulate a specific enzymatic activity (43), as we have done for the anti-HCMV activity of SIRT2 inhibitors (Figure 4F, Table 2 and Supplemental Figure 6). Six structurally distinct SIRT2-targeting compounds reduced the yield of HCMV in spread assays, arguing that SIRT2 modulation is a key element of the antiviral activity.

It is conceivable that these compounds have off-target activities that impact viral growth, perhaps via effects on additional members of the SIRT family. However, this possibility seems unlikely, because the thioacyl lysine, TM, has been tested in vitro against all seven SIRTs and is highly selective for SIRT2 (47). Further, FLS-359 (Figure 1C), AGK2 (70), MIND4 (39) and SirReal2 (50) are highly selective for SIRT2 versus their most closely related family members, SIRT1 and 3 (71).

It is not clear why the anti-HCMV activity of FLS-359 (0.5 μM; Figure 4F) appears to be more potent than its in vitro activity on purified SIRT2 (3.3 μM; Figure 1C). Intracellular SIRT2 is produced from three splice variants (72), modified by phosphorylations and acetylations (73–75), and associates with numerous other cellular proteins (76). These variations, modifications and associations might make SIRT2 more or less susceptible to inhibition by the drug. Alternatively, the compound might accumulate preferentially in a cellular compartment where a key target protein resides. It is also possible that a secondary target of the drug contributes to its antiviral activity or a more active metabolite is generated within cells. Finally, it is conceivable

412 that inhibition of SIRT2 modulates multiple pathways required for efficient viral replication,
413 amplifying the antiviral effect of the drug.

414 Our work highlights the broad-spectrum antiviral activity of FLS-359 (Table 1), which
415 inhibits the replication of both RNA and DNA viruses. The IC_{50}s for inhibition of the different
416 viruses tested range from 0.3 μM for SARS-CoV-2 to 6.7 μM for respiratory syncytial virus.
417 This range of sensitivities might result from testing in different cell types with different antiviral
418 readouts. It is also possible that different SIRT2-controlled post-translational modifications
419 impact different viruses to a greater or lesser extent and the antiviral mechanisms vary across a
420 range of pathogens. This data set clearly illustrates the broad-spectrum activity of this class of
421 inhibitors, a potentially invaluable feature of antivirals in immunosuppressed populations and as
422 new pathogens emerge and evolve in the human population.

423 How does SIRT2 inhibition antagonize HCMV replication? As noted above, HCMV
424 infection induces profound alterations to the cytoplasmic and nuclear acetylomes, including
425 changes to viral and cellular transcriptional regulatory proteins (15). Some of these changes
426 likely support viral growth and spread, by facilitating viral replication processes or by reducing
427 the cellular protective response. As a consequence, drugs that modulate the infected-cell
428 acetylome, and more broadly the infected cell acylome, have potential to create an environment
429 that antagonizes viral replication.

430 Although SIRT2 is predominately cytoplasmic, it shuttles between the nucleus and
431 cytoplasm, acting in both compartments (77). FLS-359 modestly reduced the accumulation of all
432 viral RNAs tested, including the UL122 and 123 RNAs (Figure 7B), arguing that it modulates
433 viral transcription or RNA stability. Expression of the UL122 and UL123 RNAs is controlled by
434 the major immediately-early promoter (MIEP), which is the primary HCMV promoter/enhancer

435 to become active following infection. Numerous cellular factors bind at the MIEP (64), and the
436 activity of any of these factors could potentially be modulated by SIRT2 inhibitors. SIRT2 also
437 acts on transcription by modulating the acetylation state of histones H3 and H4 (78, 79).
438 Although SIRT2 inhibition could lead to hyperacetylation of HCMV chromatin, a state that
439 generally favors transcriptional activation, an indirect consequence, such as enhanced expression
440 of a cell-coded repressor, could inhibit viral transcription. Reduced accumulation of the major
441 immediate-early proteins could then reduce the expression of all downstream viral RNAs –
442 similar to what was observed (Figure 7B). Changes in acetylation status of virus-coded factors,
443 such as pUL26, where an acetylation mimic (K203Q) inhibited virus production (15), could also
444 play a role.
445 FLS-359 also reduced intracellular viral DNA accumulation (Figure 8B), a likely
446 consequence of reduced UL44, UL54, UL57 and RNA4.9 RNA expression (Figure 7B and C).
447 pUL44 and pUL54 are subunits of the viral DNA polymerase, pUL57 is a single-stranded DNA-
448 binding protein required for viral DNA replication and RNA4.9 is a non-coding RNA that forms
449 an R-loop at the viral origin of DNA replication and is required for efficient viral DNA
450 accumulation (65). However, the relatively modest ~3-fold reduction in intracellular viral DNA
451 levels (Figure 8B) doesn't account for the >1000-fold reduction in infectious virus (Figure 8C)
452 caused by treatment with FLS-359 over the course of 72h. A second experiment recorded an
453 ~70-fold reduction in extracellular virus particles and viral infectivity was again reduced by
454 >1600-fold (Figure 8E). Thus, the number of virus particles as well as their infectivity are both
455 impacted by the drug. Reduced levels of viral proteins could interfere with efficient DNA
456 packaging into capsids, and export of mature enveloped virions. FLS-359 could also interfere
457 with the production of infectious virions by perturbing the microtubule network. Consistent with

458 the role of SIRT2 in α-tubulin deacetylation (45), FLS-359 can induce hyperacetylation of α-
459 tubulin (Supplemental Figure 1A). Altered acetylation of α-tubulin K40 has potential to
460 modulate microtubule activity (80), which in turn is critical for structure (81) and function (82)
461 of the HCMV assembly zone, the viral organelle in which capsids are assembled into virions
462 (83). Further, very long chain fatty acids are required for infectivity of virus particles (84) and
463 SIRT2 inhibition impacts lipid synthesis (85), so it's possible that an effect of FLS-359 on fatty
464 acid synthesis reduces the infectivity of HCMV progeny. Additional viral processes, such as
465 nuclear egress of capsids, which is controlled by lamin B1 acetylation (15), might also be
466 impacted by SIRT2 inhibition. Finally, in stressed tumor cells SIRT2 inhibition has been shown
467 to activate p53 (86), induce degradation of overexpressed c-Myc (46, 47) and block full
468 activation of the PI3 kinase-Akt pathway (87) - any of which could potentially reduce the
469 production of infectious viral progeny. Although further studies are needed to more fully
470 appreciate the mode of FLS-359 antiviral action, it appears likely that it's anti-HCMV
471 mechanism is multifactorial, and the multiple components likely speak to its broad-spectrum
472 antiviral activity and strongly predict that drug-resistant mutants will not evolve.
473 Will SIRT2 inhibitors prove to be well tolerated in humans? Mice appeared healthy and
474 alert and did not lose weight during our anti-HCMV studies; SIRT2 (30) and SIRT2/3 (31)
475 knockout mice are healthy; and EX-527, which is selective for SIRT1 but also has anti-SIRT2
476 activity (88), is well tolerated in humans (89). Further, the acute nature of many viral infections
477 will require short term treatments, mitigating possible long-term toxicity.
478 The broad-spectrum antiviral activity of SIRT2 inhibitors will likely find utility in
479 multiple clinical applications. Treatment of viral disease in transplant patients is a prime
480 example. These immunosuppressed patients have heightened susceptibility to environmental

pathogens as well as adventitious agents traveling with donor tissues or resident in the recipient, including herpesviruses, polyomaviruses, respiratory viruses, hepadnaviruses and emerging viruses (8, 9, 90, 91). We have already determined that several of these viral agents are inhibited by FLS-359, including HCMV (Figure 4), which continues to threaten transplant recipients in spite of effective direct-acting therapies. EBV (Figure 3), HBV, respiratory viruses that include influenza and now SARS-CoV-2, and other newly emerging agents such as Zika virus are also inhibited by FLS-359 (Table 1). A host-targeted, broad-spectrum drug should improve outcomes, especially for transplant patients undergoing antiviral prophylaxis.

In sum, FLS-359 is a representative of a new family of SIRT2 modulators. Its broad-spectrum and multifaceted antiviral activity illustrates its potential as a host-targeted antiviral with utility in treatment of numerous viral diseases and sets the stage for further understanding of how epigenetic mechanisms impact the growth and spread of multiple viral pathogens.

Methods

SIRT2 thermal stability assay. Equal volumes of 2x FLS-359 and 2x human $SIRT2^{2-352}$ (GenScript) in binding buffer (20 mM PIPES pH 7.4, 100 mM NaCl, 0.005% Tween, 10 μM 1-anilino-8-naphthalenesulfonate) were added to PCR plates (BioRad, Hard-Shell 384, black well), overlayed with silicon oil and centrifuged (600xg, 20 sec). Thermal melt data was collected using custom instrumentation (Fluorescence Innovations), with either 405 nm or 532 nm laser excitation and fluorescence lifetime emission to measure total well fluorescence and fluorescence lifetime as a function of temperature. Data was treated as described (37) to determine the midpoint transition, T_m.

SIRT deacylase assay. Human SIRT deacylase activity was measured in assay buffer (50 mM Tris, pH 8.0, 137 mM NaCl, 2.7 mM KCl, 1 mM $MgCl_2$, 1 mg/ml BSA) containing purified, recombinant $SIRT2^{2-389}$, $SIRT1^{1-747}$ or $SIRT3^{1-400}$ protein (GenScript); acetylated (Ac-H_3K_9WW: QTARK^{Ac}STGGKAPRWW-NH_2) or myristoylated (Myr-H_3K_9WW: QTARK^{Myr}STGGKAPRWW-NH_2) peptide (GenScript); NAD^+ and inhibitors. Reactions were initiated by adding SIRT protein, and aliquots were quenched with 1% formic acid after 10 min at 37°C. Reaction products (deacetylated peptide ions or Ac-ADPribose) were detected using Rapidfire-High Throughput Mass Spectrometry (PureHoney Technologies). Deacetylated peptide substrate (Genscript) and Ac-ADPribose (Toronto Research Chemicals) were used as controls in detection reactions.

X-ray structure determination. The study was performed at Crelux, GmbH. $SIRT2^{56-356}$ was used for crystallization; a hexahistidine tag used for purification was removed prior to crystallization. Crystals of SIRT2 in complex with FLS-359 were obtained using hanging-drop vapour diffusion set-ups. SIRT2 (21.9 mg/ml; 50 mM Hepes-NaOH, 150 mM NaCl, pH 8.0) was

pre-incubated with 3.6 mM (5.7-fold molar excess) of FLS-359 for 1h. A 1 µl aliquot of the protein solution was then mixed with 2 µl of reservoir solution (0.1 M Hepes-NaOH pH 6.6, 0.3 M Li_2SO_4, 21 % (w/v) PEG 3350) and streak seeded before being equilibrated at 20°C over 0.2 ml of reservoir solution. Well-diffracting crystals grew as thick aggregates of thin plates and were mounted within 19 days.

For data collection, crystals were cryo-protected by the addition of ethylene glycol to a concentration of 20% (v/v) to the crystallization drop before mounting. Single thin plates were isolated for data collection. A complete 1.8 Å data set of a SIRT2/FLS-359 single crystal was collected at Petra III (Hamburg, DE, beamline P11) (Supplemental Table 1), and the data were integrated, analyzed and scaled by XDS (92) (within the autoPROC pipeline (93)), Pointless (94) and Aimless (95), respectively.

For structure determination and refinement, molecular replacement was done using a CRELUX reference structure of SIRT2 as a starting model. Several rounds of alternating manual re-building and refinement with REFMAC5 (96) resulted in the final model (Supplemental Table 1). Atomic displacement factors were modelled with a single isotropic B-factor per atom, except for selected cysteine sulfur atoms for which residual electron density after isotropic refinement indicated an anisotropic behavior, as well as for the Zn^{++} atom in chain A. Non-crystallographic symmetry restraints were used throughout the refinement cycles.

Computational superpositioning predictions employed the Glide module of Schrödinger release 2022-4. The following SIRT2 structures were tested for predicted interactions with FLS-359: PDB ID 4RMI and 4RMG (50), 3ZGO (51), 4R8M (97), 4X3P (98).

Coordinates and structure factors of the SIRT2/FLS-359 complex have been deposited in the Protein Data Bank (PDB ID 7T1D).

548 *Cells, viruses and reagents.* Human embryonic lung fibroblasts (MRC-5; ATCC CCL-
549 171) were maintained in DMEM with 10% FBS. The type I B-lymphoma cell line, Akata (53),
550 and MDA-MB-231 breast adenocarcinoma cells (ATCC HTB-26) were cultured in RPMI 1640
551 medium with 10% FBS. HepG2 hepatocellular carcinoma cells (ATCC HB-8065) were
552 propagated in DMEM with 10% FBS. TB40/E-mCherry-UL99eGFP virus was described
553 previously (74), and it was titered by $TCID_{50}$ assay on MRC-5 cells (99). FLS-359 was
554 synthesized as described in US Patent Application US20210139475A1. ^{1}H NMR was consistent
555 with the structure, and purity was determined to be >97% by reversed phase HPLC. Ganciclovir
556 and AGK2 (Sigma), letermovir (MedChem Express), SirReal2 and MIND4
557 (Chembridge/Hit2Lead), AK-7 (Cayman Chemical) and TM (Abmole) were stored at -20°C as
558 10 mM stocks in DMSO.
559 *Assays for FLS-359 antiviral activity*. SARS-CoV-2 (strain USA-WA1/2020) was
560 assayed on Calu3 cells by qRT-PCR quantitation of extracellular viral genomes using remdesivir
561 as an antiviral control at USAMRIID. Zika virus (strain DAK41525) was assayed on human
562 foreskin fibroblasts (HFFs) by immunofluroescence assay detecting a viral antigen using
563 amodiaquine as an antiviral control at USAMRIID. HCMV (strain TB40/E) was assayed on
564 MRC-5 fibroblasts by spread assay using ganciclovir and letermovir as antiviral controls (Figure
565 4). Influenza A (strain A/California/07/2009) was assayed on differentiated normal human
566 bronchial epithelial (dNHBE) cells by yield reduction assay using ribavirin as an antiviral control
567 by a DMID contractor. Betacoronavirus 1 (strain OC43) was assayed on MRC-5 fibroblasts in a
568 CPE inhibition assay at Evrys Bio. Junin virus (strain Candid 1) was assayed on MRC-5
569 fibroblasts by immunofluorescence assay detecting a viral antigen using RIID E-1 as an antiviral
570 control at USAMRIID. Hepatitis B virus (genotype D, subtype ayw) was assayed on primary

571 human hepatocytes (PHHs) by monitoring viral rcDNA using tenofovir as an antiviral control at
572 ImQuest Biosciences. Epstein-Barr virus (EBV, strain Akata) was assayed on Akata BL cells
573 activated by treatment with anti-IgG and then monitoring viral gp350 expression using
574 phosphoacetic acid (PAA) as an antiviral control (Fig. 3). Respiratory syncytial virus (strain
575 Long) was assayed on MRC-5 fibroblasts by immunofluorescence assay detecting multiple viral
576 antigens using ribavirin as an antiviral control at RetroVirox. Assays were performed in triplicate
577 to determine IC_{50}s.

578 *Assay for HCMV spread.* Confluent MRC-5 cultures were infected with TB40/E-
579 mCherry-UL99eGFP (0.01 IU/cell). Drugs were added after a 1h adsorption period using a
580 Tecan D300e dispenser, and the DMSO concentration was normalized to 0.5% across wells. At 7
581 dpi, fluorescent images were captured using a BioTek Cytation 3 Multi-Mode Reader and
582 analyzed using Agilent BioTek Gen5 software to calculate infected cell area. Uninfected, drug-
583 treated cultures were fixed with 4% paraformaldehyde, stained with 4′,6-diamidino-2-
584 phenylindole (DAPI), imaged and analyzed to determine nuclei counts.

585 *Protein, RNA and DNA analysis.* Proteins were analyzed by western blot as described
586 (100) using anti-mCherry (1:1,000, Abcam EPR20579), anti-IE1 (1:100, clone 1B12 (101)), anti-
587 acetyl-alpha-tubulin (K40 (1:10,000, Sigma T7451), anti-cMyc (1:2,000, Abcam Y69), anti-beta-
588 actin (1:10,000, Sigma A5441) and anti-alpha-tubulin (1:10,000, Sigma DMA1) primary
589 antibodies, plus IRDye 680RD anti-mouse or IRDye 800CW anti-rabbit (1:20,000, LI-COR)
590 secondary antibodies. RNA and DNA were analyzed by quantitative PCR assay as described
591 (100) using primers listed in Supplemental Table 3.

592 *Analysis of mouse PK parameters and tolerability.* FLS-359 was formulated as a
593 suspension at 5 mg/mL in 0.5% methylcellulose (cP 25) + 0.5% Tween 80 (Sigma) in sterile

water and vortexed and/or sonicated immediately prior to p.o. administration. The PK study used fed, female BALB/c mice (22 g, n = 3/time point). Blood samples (~30 µL via saphenous vein puncture) were taken at 0.25, 0.5, 1, 2, 4, 8 and 24h. A standard curve was prepared in control plasma using FLS-359 (0.01 to 10 µg/mL) in terfenadine sovlent (50 ng/mL in methanol/acetonitrile 1:1 v/v). The lower limit of quantification was 10 ng/mL. An aliquot of 10 µL plasma sample was mixed with 10 µL terfenadine solvent plus 2 µL methanol. An additional 200 µL of terfenadine solvent was added and the resulting mixture was vortexed for 1 min and centrifuged at 4000 rpm for 15 min. The supernatant was diluted 10x with methanol/water (1:1, v/v, with 0.1% formic acid) and 2 µL aliquots were analyzed using a QTRAP 4000 LC-MS/MS System (Sciex) with a C18 column (Kinetex). Pharmacokinetic parameters were determined by using the noncompartmental analysis tool in WinNonlin (Certara).

To assess the tolerability of FLS-359, female NOD/Shi-scid/IL-2Rγ^{null} (NOG) mice were treated with 50 mg/kg/p.o./b.i.d. for 14 days. Mice had free access to food and water and were evaluated for morbidity and mortality twice daily. Body weights and food consumption were recorded once per day prior to the morning dosing. Detailed clinical observations were made 1 – 2h after the morning compound administration and once 5 – 6h after the morning observation.

Mouse gelfoam-fibroblast model for anti-HCMV activity. For the mouse gelfoam model (59, 67), MRC-5 cells were infected with HCMV TB40/E-mCherry-UL99eGFP (0.05 IU/cell). On the same day, sterile gelfoam (SURGIFOAM Absorbable Gelatin Sponge, U.S.P.) was aseptically cut into 1.2 cm x 0.5 cm x 0.7 cm pieces, and transferred into a sterile dish containing DMEM. Infected cultures and gelfoam pieces were incubated at 37°C for 24h. Then, infected cells were harvested, counted, and 1 x 10^6 cells in medium (30 µL) were slowly added to the gelfoam pieces in a 24-well non-tissue culture treated plate. Seeded gelfoams were incubated for

3 h at 37°C, and then 1 mL of medium was added to each gelfoam and incubated at 37°C for 3 days. On the day of gelfoam implant, 18-week-old male and female NOD.Cg-*Prkdc*^{scid}*Il2rg*^{tm1Sug}*/JicTac* mice (CIEA NOG, Taconic Biosciences) were anesthetized using isoflurane (Patterson Veterinary), the dorsal area above the hip region was shaved and sterilized with Betadine (Purdue Products) and 70% ethanol, and the gelfoam was inserted beneath the skin and incisions were closed. FLS-359 (50 mg/kg, p.o., b.i.d.), valganciclovir (50 mg/kg, p.o., q.d.) or diluent (0.5% methyl cellulose + 0.5% Tween 80) were administered, beginning immediately after implantation. On day 11, mice were euthanized and the gelfoams were harvested, homogenized, clarified by centrifugation at 14,000 rpm for 5 min at 4ºC, and virus in the supernatant was quantified by $TCID_{50}$.

Human lung-only mouse (LoM) model for anti-HCMV activity. LoM were generated as previously decribed (68, 69). In brief, LoM were constructed by implanting two pieces of human lung tissue (Advanced Bioscience Resources) subcutaneously into the back of male and female NOD.Cg-Prkdc^{scid} ll2rg^{tm1Wjl}/SzJ mice (NSG, Jackson Laboratory). Expansion of the implants was monitored by palpation. Anesthetized mice were exposed to HCMV by direct injection of HCMV TB40/E (4.25×10^5 IU) into the implants in a total volume of 100 µL. Mice received vehicle control (0.5% methyl cellulose, 0.5% Tween 80; p.o., b.i.d), FLS-359 (50 mg/kg in vehicle; p.o., b.i.d.) or ganciclovir (100 mg/kg; i.p., q.d.) beginning 2h before infection. Human lung implants were harvested at 17 days post-infection and flash frozen. Subsequently, implants were thawed, homogenized and virus load was measured by $TCID_{50}$ assay.

Statistics. Quantitative results are shown as mean ± SD of independent experiments as noted in figure legends. Statistical significance was evaluated using GraphPad Prism 8

(GraphPad Software). Efficacy readouts in animal studies were compared between treatment groups by Kruskal Wallis test, followed by one-sided Dunn's multiple comparison test.

Study approval. Mouse studies were carried out in compliance with the NIH Guide for the Care and Use of Laboratory Animals according to protocols approved by Institutional Animal Care and Use Committees: Bioduro Beijing Co. (Protocol BD-201709136, mouse PK); the Trudeau Institute (Protocol 19-002, HCMV Gelfoam); and the University of North Carolina-Chapel Hill (Protocol 20-235, HCMV LoM).

Author contributions

KLR, SR, MJT, JLK, LT, AB, CD, WWR, AVW, JVG, MAL, TS, EAM, and LWC designed research studies; KLR, SR, MJT, LT, AB, AVW and CD conducted experiments and acquired data; KLR, SR, MJT, JLK, LT, AB, CD, WWR, AVW, JVG, MAL, TS, EAM, and LWC analyzed data; KLR, SR, MJT, JLK, LT, AVW, AB, WWR, AW, JVG, MAL, TS, JRT, EAM, and LWC contributed to writing the manuscript and/or preparing figures.

Acknowledgments

We thank Emre Koyuncu (Cresenta Biosciences) for insights into the antiviral activities of sirtuins; John Denu (University of Wisconsin) for advice on the biochemistry of sirtuin 2; Quint Kückelhaus (Crelux) for running SIRT2/FLS-359 crystalizations, Karine Röwer (Crelux) for SIRT2/FLS-359 X-ray structure determination and Nieng Yan (Princeton University) for advice on X-ray crystallography; Youngwok Kim (Evrys Bio) and Sheli Radoshitsky (USAMRIID) for performing in vitro antiviral assays; Deborah Duso and Tricia Hart (Trudeau Institute) for implanting and harvesting gelfoams, gavaging mice and doing $TCID_{50}$ assays; and Matthew Cole (Trudeau Institute) for preparing virus stocks and infecting fibroblasts for implantation in gelfoams. Evrys Bio utilized the non-clinical and pre-clinical services program offered by NIAID. These studies were funded in part by grants from NIH to Evrys Bio (R43-AI110048, R44-AI122488, R43-AI114079, and R44-AI114079) and Micah A. Luftig (R01-CA140337) and a contract to Evrys Bio from the Department of Defense (W911QY18P0300). Evrys Bio has issued patents and pending applications claiming composition of matter for SIRT2 modulators.

References

1. Feld JJ et al. Sofosbuvir and Velpatasvir for HCV Genotype 1, 2, 4, 5, and 6 Infection. *N. Engl. J. Med.* 2015;373(27):2599–2607.

2. Hussain M, Galvin H, Haw TY, Nutsford A, Husain M. Drug resistance in influenza A virus: the epidemiology and management. *Infect. Drug Resist.* 2017;Volume 10:121–134.

3. Brown AJ et al. Broad spectrum antiviral remdesivir inhibits human endemic and zoonotic deltacoronaviruses with a highly divergent RNA dependent RNA polymerase. *Antiviral Res.* 2019;169:104541.

4. Bösl K et al. Common Nodes of Virus–Host Interaction Revealed Through an Integrated Network Analysis. *Front. Immunol.* 2019;10. doi:10.3389/fimmu.2019.02186

5. Ianevski A et al. Novel activities of safe-in-human broad-spectrum antiviral agents. *Antiviral Res.* 2018;154:174–182.

6. Adalja A, Inglesby T. Broad-Spectrum Antiviral Agents: A Crucial Pandemic Tool. *Expert Rev. Anti. Infect. Ther.* 2019;17(7):467–470.

7. Bekerman E, Einav S. Combating emerging viral threats. *Science (80-.).* 2015;348(6232):282–283.

8. Taneja A, Chewning JH, Saad A. Viral infections after allogeneic hematopoietic stem cell transplant. *Adv. CELL GENE Ther.* 2019;2(2):e43.

9. Fishman JA. Infection in Organ Transplantation. *Am. J. Transplant.* 2017; doi:10.1111/ajt.14208

10. Svinkina T et al. Deep, quantitative coverage of the lysine acetylome using novel anti-acetyl-lysine antibodies and an optimized proteomic workflow. *Mol. Cell. Proteomics* 2015;14(9):2429–2440.

11. Choudhary C, Weinert BT, Nishida Y, Verdin E, Mann M. The growing landscape of lysine acetylation links metabolism and cell signalling.. *Nat. Rev. Mol. Cell Biol.* 2014;15(8):536–50.

12. Narita T, Weinert BT, Choudhary C. Functions and mechanisms of non-histone protein acetylation. *Nat. Rev. Mol. Cell Biol.* 2019;20(3):156–174.

13. Jeng MY, Ali I, Ott M. Manipulation of the host protein acetylation network by human immunodeficiency virus type 1.. *Crit. Rev. Biochem. Mol. Biol.* 2015;50(4):314–25.

728 14. Giese S et al. Role of influenza A virus NP acetylation on viral growth and replication. *Nat.*
729 *Commun.* 2017;8(1):1259.
730 15. Murray LA, Sheng X, Cristea IM. Orchestration of protein acetylation as a toggle for cellular
731 defense and virus replication.. *Nat. Commun.* 2018;9(1):4967.
732 16. Li T, Diner BA, Chen J, Cristea IM. Acetylation modulates cellular distribution and DNA
733 sensing ability of interferon-inducible protein IFI16. *Proc. Natl. Acad. Sci.* 2012;109(26):10558–
734 10563.
735 17. Chen L -f. Acetylation of RelA at discrete sites regulates distinct nuclear functions of NF-
736 kappaB. *EMBO J.* 2002;21(23):6539–6548.
737 18. Sharma A, Mahur P, Muthukumaran J, Singh AK, Jain M. Shedding light on structure,
738 function and regulation of human sirtuins: a comprehensive review. *3 Biotech* 2023;13(1):29.
739 19. Feldman JL, Dittenhafer-Reed KE, Denu JM. Sirtuin Catalysis and Regulation. *J. Biol. Chem.*
740 2012;287(51):42419–42427.
741 20. Feldman JL, Baeza J, Denu JM. Activation of the protein deacetylase SIRT6 by long-chain
742 fatty acids and widespread deacylation by Mammalian Sirtuins. *J. Biol. Chem.*
743 2013;288(43):31350–31356.
744 21. Goodwin ML, Gladden LB, Nijsten MWN, Jones KB. Lactate and Cancer: Revisiting the
745 Warburg Effect in an Era of Lactate Shuttling. *Front. Nutr.* 2015;1:doi:
746 10.3389/fnut.2014.00027.
747 22. Shenk T, Alwine JC. Human Cytomegalovirus: Coordinating Cellular Stress, Signaling, and
748 Metabolic Pathways. *Annu. Rev. Virol.* 2014;1(1):355–374.
749 23. Michishita E, Park JY, Burneskis JM, Barrett JC, Horikawa I. Evolutionarily Conserved and
750 Nonconserved Cellular Localizations and Functions of Human SIRT Proteins. *Mol. Biol. Cell*
751 2005;16(10):4623–4635.
752 24. Koyuncu E et al. Sirtuins are evolutionarily conserved viral restriction factors. *MBio*
753 2014;5(6):doi: 10.1128/mBio.02249-14.
754 25. Hackett BA et al. Sirtuin Inhibitors Are Broadly Antiviral against Arboviruses. *MBio*
755 2019;10(4). doi:10.1128/mBio.01446-19
756 26. Mao G et al. Suppressive effects of sirtinol on human cytomegalovirus (hCMV) infection and

hCMV-induced activation of molecular mechanisms of senescence and production of reactive oxygen species. *Mech. Ageing Dev.* 2016;158:62–69.

27. Outeiro TF et al. Sirtuin 2 inhibitors rescue α-synuclein-mediated toxicity in models of Parkinson's disease. *Science (80-.).* 2007;317(5837):516–519.

28. Yu H-B et al. AGK2, A SIRT2 Inhibitor, Inhibits Hepatitis B Virus Replication In Vitro And In Vivo. *Int. J. Med. Sci.* 2018;15(12):1356–1364.

29. Piracha ZZ et al. Sirtuin 2 Isoform 1 Enhances Hepatitis B Virus RNA Transcription and DNA Synthesis through the AKT/GSK-3β/β-Catenin Signaling Pathway. *J. Virol.* 2018;92(21):doi: 10.1128/JVI.00955-18.

30. Ciarlo E et al. Sirtuin 2 Deficiency Increases Bacterial Phagocytosis by Macrophages and Protects from Chronic Staphylococcal Infection.. *Front. Immunol.* 2017;8:1037.

31. Heinonen T et al. Dual Deletion of the Sirtuins SIRT2 and SIRT3 Impacts on Metabolism and Inflammatory Responses of Macrophages and Protects From Endotoxemia. *Front. Immunol.* 2019;10(November):1–16.

32. Limaye AP, Babu TM, Boeckh M. Progress and Challenges in the Prevention, Diagnosis, and Management of Cytomegalovirus Infection in Transplantation. *Clin. Microbiol. Rev.* 2020;34(1). doi:10.1128/CMR.00043-19

33. Kotton CN. Updates on antiviral drugs for cytomegalovirus prevention and treatment.. *Curr. Opin. Organ Transplant.* 2019;24(4):469–475.

34. Griffiths P, Reeves M. Pathogenesis of human cytomegalovirus in the immunocompromised host. *Nat. Rev. Microbiol.* 2021;19(12):759–773.

35. San-Juan R et al. Epstein-Barr virus-related post-transplant lymphoproliferative disorder in solid organ transplant recipients. *Clin. Microbiol. Infect.* 2014;20:109–118.

36. Bamoulid J et al. Subclinical Epstein-Barr virus Viremia among adult renal transplant recipients: Incidence and consequences. *Am. J. Transplant.* 2013; doi:10.1111/ajt.12009

37. Matulis D, Kranz JK, Salemme FR, Todd MJ. Thermodynamic Stability of Carbonic Anhydrase: Measurements of Binding Affinity and Stoichiometry Using ThermoFluor. *Biochemistry* 2005;44(13):5258–5266.

38. Outeiro TF et al. Sirtuin 2 Inhibitors Rescue α-Synuclein-Mediated Toxicity in Models of

786 Parkinson's Disease. *Science (80-.).* 2007;317(5837):516–519.
787 39. Quinti L et al. SIRT2- and NRF2-Targeting Thiazole-Containing Compound with Therapeutic
788 Activity in Huntington's Disease Models. *Cell Chem. Biol.* 2016;23(7):849–861.
789 40. Huang H et al. Lysine benzoylation is a histone mark regulated by SIRT2. *Nat. Commun.*
790 2018;9(1):3374.
791 41. Galleano I, Schiedel M, Jung M, Madsen AS, Olsen CA. A Continuous, Fluorogenic Sirtuin 2
792 Deacylase Assay: Substrate Screening and Inhibitor Evaluation. *J. Med. Chem.* 2016;59(3):1021–
793 1031.
794 42. Spiegelman NA et al. Direct Comparison of SIRT2 Inhibitors: Potency, Specificity, Activity-
795 Dependent Inhibition, and On-Target Anticancer Activities. *ChemMedChem* 2018;13(18):1890–
796 1894.
797 43. Lin H. Substrate-selective small-molecule modulators of enzymes: Mechanisms and
798 opportunities.. *Curr. Opin. Chem. Biol.* 2022;72:102231.
799 44. Kudo N, Ito A, Arata M, Nakata A, Yoshida M. Identification of a novel small molecule that
800 inhibits deacetylase but not defatty-acylase reaction catalysed by SIRT2. *Philos. Trans. R. Soc. B*
801 *Biol. Sci.* 2018;373(1748):20170070.
802 45. North BJ, Marshall BL, Borra MT, Denu JM, Verdin E. The Human Sir2 Ortholog, SIRT2, Is an
803 NAD+-Dependent Tubulin Deacetylase. *Mol. Cell* 2003;11(2):437–444.
804 46. Liu PY et al. The histone deacetylase SIRT2 stabilizes Myc oncoproteins. *Cell Death Differ.*
805 2013;20(3):503–514.
806 47. Jing H et al. A SIRT2-Selective Inhibitor Promotes c-Myc Oncoprotein Degradation and
807 Exhibits Broad Anticancer Activity. *Cancer Cell* 2016;29(3):297–310.
808 48. Wang. An overview of Sirtuins as potential therapeutic target: Structure, function and
809 modulators. *Eur J Med Chem* 2019;161:48–77.
810 49. Moniot S, Weyand M, Steegborn C. Structures, Substrates, and Regulators of Mammalian
811 Sirtuins – Opportunities and Challenges for Drug Development [Internet]. *Front. Pharmacol.*
812 2012;3. doi:10.3389/fphar.2012.00016
813 50. Rumpf T et al. Selective Sirt2 inhibition by ligand-induced rearrangement of the active site.
814 *Nat. Commun.* 2015;6(1):doi: 10.1038/ncomms7263.

815 51. Moniot S, Schutkowski M, Steegborn C. Crystal structure analysis of human Sirt2 and its
816 ADP-ribose complex. *J. Struct. Biol.* 2013;182(2):136–143.
817 52. Wang T et al. Recent Progress on the Discovery of Sirt2 Inhibitors for the Treatment of
818 Various Cancers. *Curr. Top. Med. Chem.* 2019;19(12):1051–1058.
819 53. Takada K et al. An Epstein-Barr virus-producer line Akata: Establishment of the cell line and
820 analysis of viral DNA. *Virus Genes* 1991;5(2):147–156.
821 54. Cifuentes-Munoz N, El Najjar F, Dutch RE. Viral cell-to-cell spread: Conventional and non-
822 conventional ways. In: *Advances in Virus Research*. 2020:85–125
823 55. Cifuentes-Muñoz N, Dutch RE, Cattaneo R. Direct cell-to-cell transmission of respiratory
824 viruses: The fast lanes. *PLOS Pathog.* 2018;14(6):e1007015.
825 56. Silva MC, Schröer J, Shenk T. Human cytomegalovirus cell-to-cell spread in the absence of an
826 essential assembly protein.. *Proc. Natl. Acad. Sci. U. S. A.* 2005;102(6):2081–6.
827 57. Nukui M, O'Connor C, Murphy E. The Natural Flavonoid Compound Deguelin Inhibits HCMV
828 Lytic Replication within Fibroblasts. *Viruses* 2018;10(11):614.
829 58. Plotkin SA, Drew WL, Felsenstein D, Hirsch MS. Sensitivity of Clinical Isolates of Human
830 Cytomegalovirus to 9-(1,3-Dihydroxy-2-Prop.oxymethyl)Guanine. *J. Infect. Dis.*
831 1985;152(4):833–834.
832 59. Lischka P et al. InVitro and In Vivo Activities of the Novel Anticytomegalovirus Compound
833 AIC246. *Antimicrob. Agents Chemother.* 2010;54(3):1290–1297.
834 60. Razonable R, Melendez D. Letermovir and inhibitors of the terminase complex: a promising
835 new class of investigational antiviral drugs against human cytomegalovirus. *Infect. Drug Resist.*
836 2015;269.
837 61. Goldner T et al. The Novel Anticytomegalovirus Compound AIC246 (Letermovir) Inhibits
838 Human Cytomegalovirus Replication through a Specific Antiviral Mechanism That Involves the
839 Viral Terminase. *J. Virol.* 2011;85(20):10884–10893.
840 62. Taylor DM et al. A Brain-Permeable Small Molecule Reduces Neuronal Cholesterol by
841 Inhibiting Activity of Sirtuin 2 Deacetylase. *ACS Chem. Biol.* 2011;6(6):540–546.
842 63. Stinski MF, Meier JL. *Immediate–early viral gene regulation and function*. 2007:
843 64. Adamson CS, Nevels MM. Bright and Early: Inhibiting Human Cytomegalovirus by Targeting

844 Major Immediate-Early Gene Expression or Protein Function. *Viruses* 2020;12(1):110.
845 65. Tai-Schmiedel J et al. Human cytomegalovirus long noncoding RNA4.9 regulates viral DNA
846 replication. *PLOS Pathog.* 2020;16(4):e1008390.
847 66. Pari GS. Nuts and Bolts of Human Cytomegalovirus Lytic DNA Replication. In: *Current Topics*
848 *in Microbiology and Immunology*. 2008:153–166
849 67. Bravo FJ, Cardin RD, Bernstein DI. A model of human cytomegalovirus infection in severe
850 combined immunodeficient mice. *Antiviral Res.* 2007;76(2):104–110.
851 68. Wahl A et al. Precision mouse models with expanded tropism for human pathogens. *Nat.*
852 *Biotechnol.* 2019;37(10):1163–1173.
853 69. Wahl A et al. SARS-CoV-2 infection is effectively treated and prevented by EIDD-2801.
854 *Nature* 2021;591(7850):451–457.
855 70. Tatum PR et al. Identification of novel SIRT2-selective inhibitors using a click chemistry
856 approach. *Bioorg. Med. Chem. Lett.* 2014;24(8):1871–1874.
857 71. Frye RA. Phylogenetic Classification of Prokaryotic and Eukaryotic Sir2-like Proteins.
858 *Biochem. Biophys. Res. Commun.* 2000;273(2):793–798.
859 72. Rack JGM, VanLinden MR, Lutter T, Aasland R, Ziegler M. Constitutive Nuclear Localization
860 of an Alternatively Spliced Sirtuin-2 Isoform. *J. Mol. Biol.* 2014;426(8):1677–1691.
861 73. Choi YH, Kim H, Lee SH, Jin Y-H, Lee KY. Src regulates the activity of SIRT2. *Biochem. Biophys.*
862 *Res. Commun.* 2014;450(2):1120–1125.
863 74. North BJ, Verdin E. Mitotic Regulation of SIRT2 by Cyclin-dependent Kinase 1-dependent
864 Phosphorylation. *J. Biol. Chem.* 2007;282(27):19546–19555.
865 75. Pereira JM et al. Infection Reveals a Modification of SIRT2 Critical for Chromatin
866 Association.. *Cell Rep.* 2018;23(4):1124–1137.
867 76. Budayeva HG, Cristea IM. Human Sirtuin 2 Localization, Transient Interactions, and Impact
868 on the Proteome Point to Its Role in Intracellular Trafficking. *Mol. Cell. Proteomics*
869 2016;15(10):3107–3125.
870 77. North BJ, Verdin E. Interphase Nucleo-Cytoplasmic Shuttling and Localization of SIRT2
871 during Mitosis. *PLoS One* 2007;2(8):e784.
872 78. Das C, Lucia MS, Hansen KC, Tyler JK. CBP/p300-mediated acetylation of histone H3 on

873 lysine 56. *Nature* 2009;459(7243):113–117.
874 79. Vaquero A. SirT2 is a histone deacetylase with preference for histone H4 Lys 16 during
875 mitosis. *Genes Dev.* 2006;20(10):1256–1261.
876 80. Janke C, Montagnac G. Causes and Consequences of Microtubule Acetylation. *Curr. Biol.*
877 2017;27(23):R1287–R1292.
878 81. Sanchez V, Greis KD, Sztul E, Britt WJ. Accumulation of virion tegument and envelope
879 proteins in a stable cytoplasmic compartment during human cytomegalovirus replication:
880 characterization of a potential site of virus assembly.. *J. Virol.* 2000;74:975–986.
881 82. Clippinger AJ, Alwine JC. Dynein mediates the localization and activation of mTOR in normal
882 and human cytomegalovirus-infected cells.. *Genes Dev.* 2012;26:2015–2026.
883 83. Alwine JC. The human cytomegalovirus assembly compartment: A masterpiece of viral
884 manipulation of cellular processes that facilitate assembluy and egress.. *PLOS Pathog.*
885 2012;8(9):e1002878.
886 84. Koyuncu E, Purdy JG, Rabinowitz JD, Shenk T. Saturated very long chain fatty acids are
887 required for the production of infectious human cytomegalovirus progeny. *PLoS Pathog*
888 2013;9(5):e1003333.
889 85. Ye X et al. Sirtuins in glucose and lipid metabolism. *Oncotarget* 2017;8(1):1845–1859.
890 86. Hoffmann G, Breitenbücher F, Schuler M, Ehrenhofer-Murray AE. A novel sirtuin 2 (SIRT2)
891 inhibitor with p53-dependent pro-apoptotic activity in non-small cell lung cancer. *J. Biol. Chem.*
892 2014;289(8):5208–5216.
893 87. Ramakrishnan G et al. Sirt2 Deacetylase Is a Novel AKT Binding Partner Critical for AKT
894 Activation by Insulin. *J. Biol. Chem.* 2014;289(9):6054–6066.
895 88. Napper AD et al. Discovery of Indoles as Potent and Selective Inhibitors of the Deacetylase
896 SIRT1. *J. Med. Chem.* 2005;48(25):8045–8054.
897 89. Westerberg G et al. Safety, pharmacokinetics, pharmacogenomics and QT
898 concentration−effect modelling of the SirT1 inhibitor selisistat in healthy volunteers. *Br. J. Clin.*
899 *Pharmacol.* 2015;79(3):477–491.
900 90. Clausen ES, Zaffiri L. Infection prophylaxis and management of viral infection. *Ann. Transl.*
901 *Med.* 2020;8(6):415–415.

902 91. Manansala M, Baughman R, Novak R, Judson M, Sweiss N. Management of
903 immunosuppressants in the era of coronavirus disease-2019. *Curr. Opin. Pulm. Med.*
904 2021;27(3):176–183.
905 92. Kabsch W et al. XDS. *Acta Crystallogr. Sect. D Biol. Crystallogr.* 2010;66(2):125–132.
906 93. Vonrhein C et al. Data processing and analysis with the autoPROC toolbox. *Acta Crystallogr.*
907 *Sect. D Biol. Crystallogr.* 2011;67(4):293–302.
908 94. Evans P. Scaling and assessment of data quality. *Acta Crystallogr. Sect. D Biol. Crystallogr.*
909 2006;62(1):72–82.
910 95. Evans PR, Murshudov GN. How good are my data and what is the resolution?. *Acta*
911 *Crystallogr. Sect. D Biol. Crystallogr.* 2013;69(7):1204–1214.
912 96. Kovalevskiy O, Nicholls RA, Long F, Carlon A, Murshudov GN. Overview of refinement
913 procedures within REFMAC 5: utilizing data from different sources. *Acta Crystallogr. Sect. D*
914 *Struct. Biol.* 2018;74(3):215–227.
915 97. Teng Y-B et al. Efficient Demyristoylase Activity of SIRT2 Revealed by Kinetic and Structural
916 Studies. *Sci. Rep.* 2015;5(1):8529.
917 98. Wang Y et al. Deacylation Mechanism by SIRT2 Revealed in the 1'-SH-2'-O-Myristoyl
918 Intermediate Structure. *Cell Chem. Biol.* 2017;24(3):339–345.
919 99. O'Connor CM, Shenk T. Human cytomegalovirus pUS27 G protein-coupled receptor
920 homologue is required for efficient spread by the extracellular route but not for direct cell-to-
921 cell spread. *J. Virol.* 2011;85(8). doi:10.1128/JVI.02442-10
922 100. Nukui M, Roche KL, Jia J, Fox PL, Murphy EA. Protein S-Nitrosylation of Human
923 Cytomegalovirus pp71 Inhibits Its Ability To Limit STING Antiviral Responses. *J. Virol.*
924 2020;94(17). doi:10.1128/JVI.00033-20
925 101. Zhu H, Shen Y, Shenk T. Human cytomegalovirus IE1 and IE2 proteins block apoptosis. *J.*
926 *Virol.* 1995;69:7960–7970.
927
928
929
930

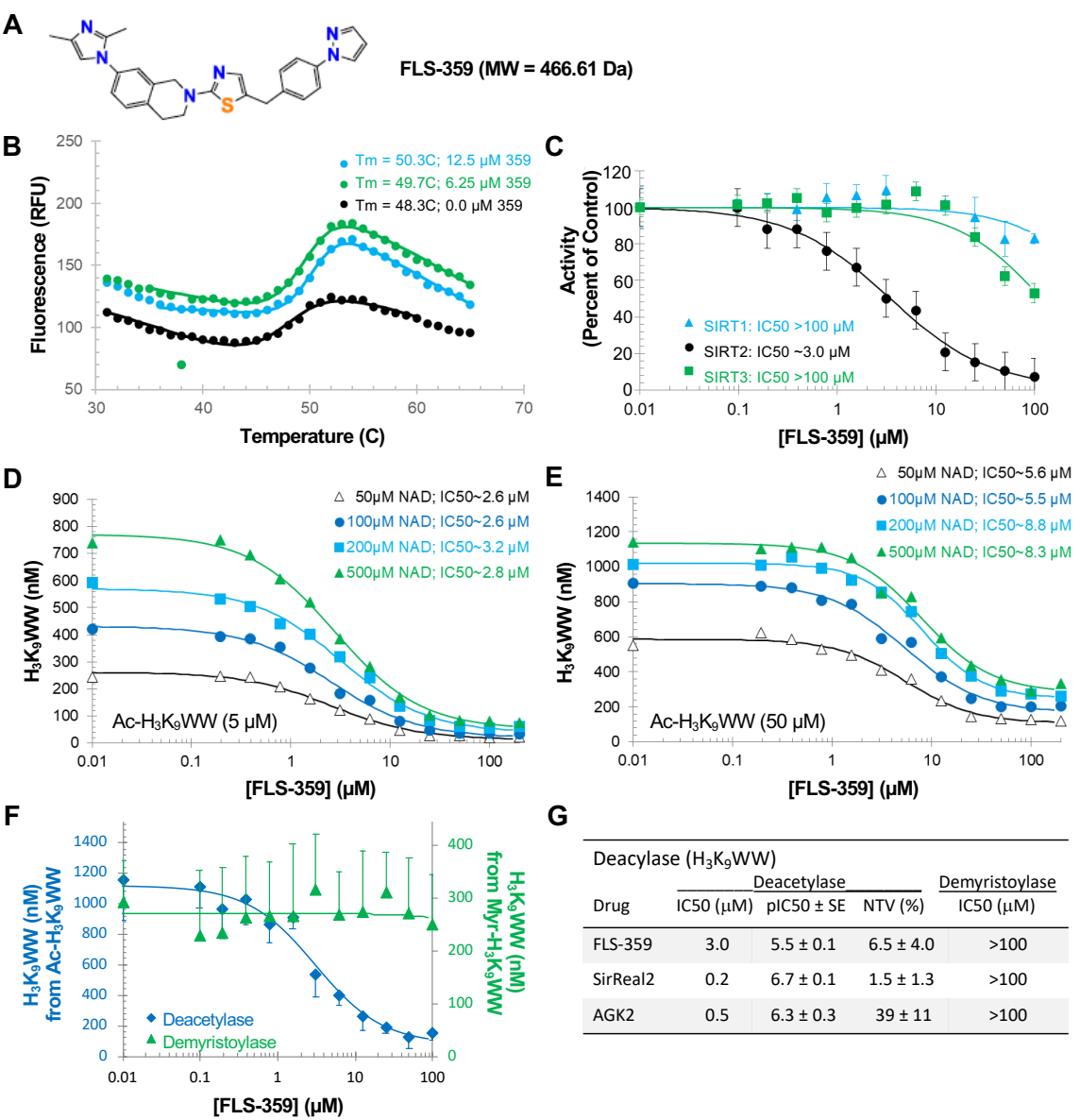

G

Deacylase (H_3K_9WW)	Deacetylase			Demyristoylase
Drug	IC50 (µM)	pIC50 ± SE	NTV (%)	IC50 (µM)
FLS-359	3.0	5.5 ± 0.1	6.5 ± 4.0	>100
SirReal2	0.2	6.7 ± 0.1	1.5 ± 1.3	>100
AGK2	0.5	6.3 ± 0.3	39 ± 11	>100

Figure 1. FLS-359 binds SIRT2, selectively reducing its catalytic activity. (**A**) Structure of FLS-359, 7-(2,4-dimethyl-1H-imidazol-1-yl)-2-(5-{[4-(1H-pyrazol-1-yl)phenyl]methyl}-1,3-thiazol-2-yl)-1,2,3,4-tetrahydroisoquinoline. (**B**) FLS-359 alters SIRT2 thermal stability. Recombinant human SIRT2$^{2\text{-}389}$ (2.5 µM) denaturation was assayed in the presence of solvent (black), 6.25 µM (green) or 12.5 µM FLS-359 (blue). (**C**) FLS-359 exhibits SIRT2-selective activity. Reactions used recombinant human SIRT1$^{1\text{-}747}$ (blue), SIRT2$^{2\text{-}389}$ (black) or SIRT3$^{1\text{-}400}$ (green) protein (n=3). (**D, E**) SIRT2 inhibition by FLS-359 is not highly dependent on substrate concentration. NAD^+ concentration was varied from K_m (50 µM) to 10x K_m (500 µM). Deacetylase assays used Ac-H_3K_9WW at K_m (5 µM, left panel) or 10x K_m (50 µM, right panel). (**F, G**) FLS-359 does not inhibit SIRT2 demyristoylase activity. Reactions used 5 µM acylated peptide (Myr-H_3K_9WW) and 500 µM NAD. (**F**) Effect of FLS-359 on SIRT2 deacetylase versus demyristolyase activity (n=3). (**G**) Table quantifying the effects of FLS-359 and anti-SIRT2 tool compounds on deacylation activities. The negative log of the IC50 (pIC50, M) and SIRT2 activity with saturating compound (Net Terminal Value, NTV), are reported as averages for triplicate measurements with standard errors. Enzymatic reactions were initiated by the addition of SIRT protein, quenched after 10 min at 37°C and deacetylated product was detected by mass spectrometry.

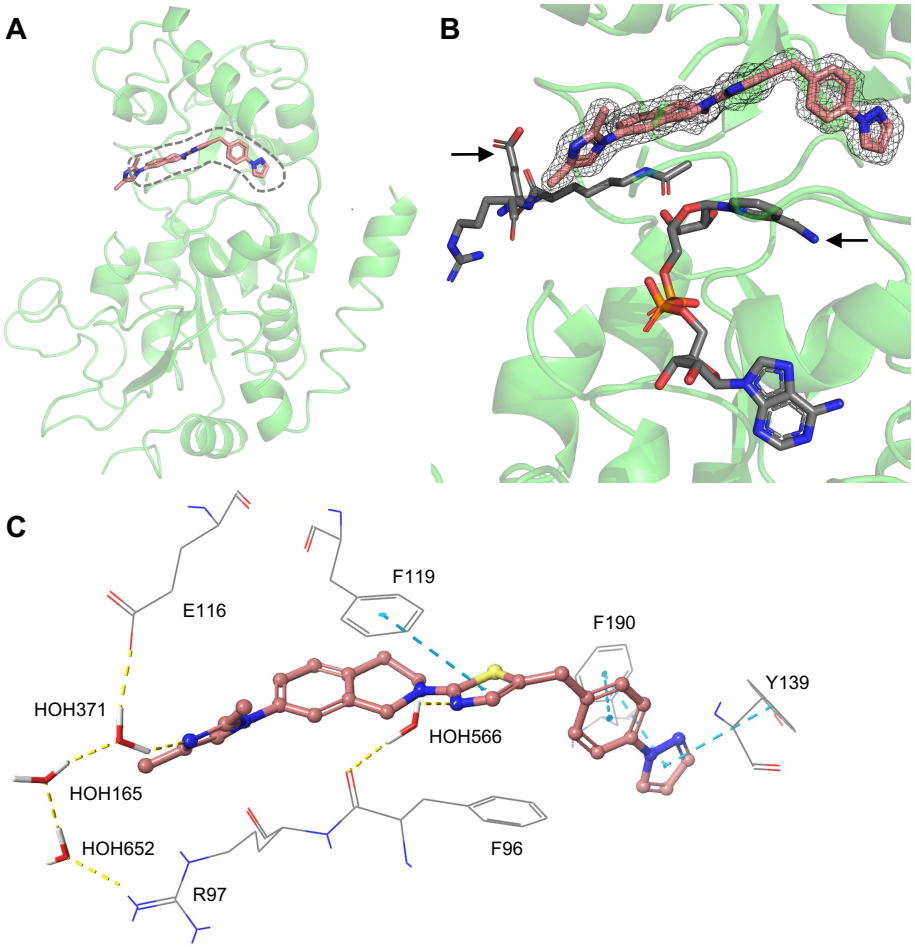

Figure 2. Co-crystal structure of FLS-359 bound to human SIRT2. (**A**) SIRT2 (green ribbon) with FLS-359 (pink carbon atoms in stick display) bound to its EC-site (dashed lines). (**B**) Superposition of SIRT2-359 with an Ac-Lys peptide (right-pointing arrow; PDB ID 4RMI) plus NAD^+ (left-pointing arrow; PDB ID 4RMG). The grey mesh over FLS-359 marks the 2fo-fc electron density map (contoured at 1.5 s) resulting from refinement of the final model with REFMAC5. (**C**) Close-up view of the SIRT2 EC-site focusing on the key FLS-359-SIRT2 interactions. Yellow-highlighted dashed lines indicate hydrogen bonds and blue dashed bonds represent **π-π** interactions.

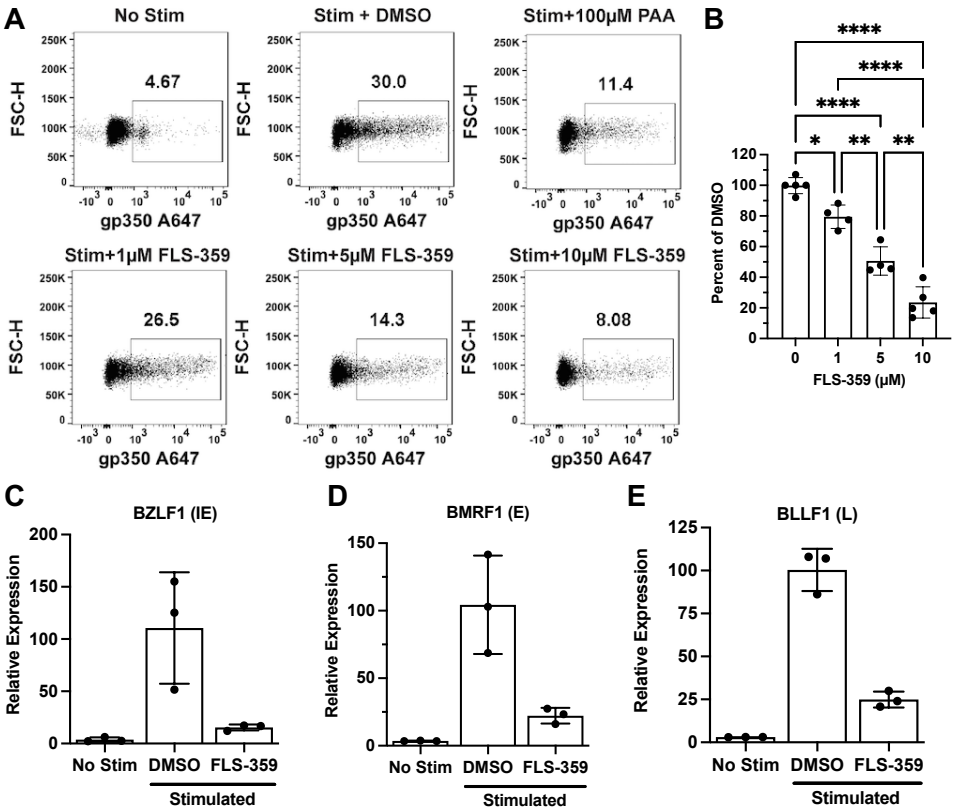

Figure 3. FLS-359 suppresses EBV lytic reactivation. (**A**) Akata BL cells were stimulated with 10 μg/mL anti-IgG and simultaneously treated with DMSO, 100 μM PAA (phosphono-acetic acid, positive control), or increasing concentrations of FLS-359 (1, 5, and 10 μM). Surface expression of the viral late gene, gp350, was measured at 24h post induction by flow cytometry. (**B**) Dot plots reporting experiments in panel A shown with mean +/- SD (n=4). (**C-E**) Dot plots reporting quantitative RT-PCR measurement of BZLF1 (IE: immediate early), BMRF1 (E: early), and BLLF1 (L: late) gene expression suppressed by FLS-359 (10 μM) in Akata BL cells induced with anti-IgG. Mean +/- SD is shown (n =3).

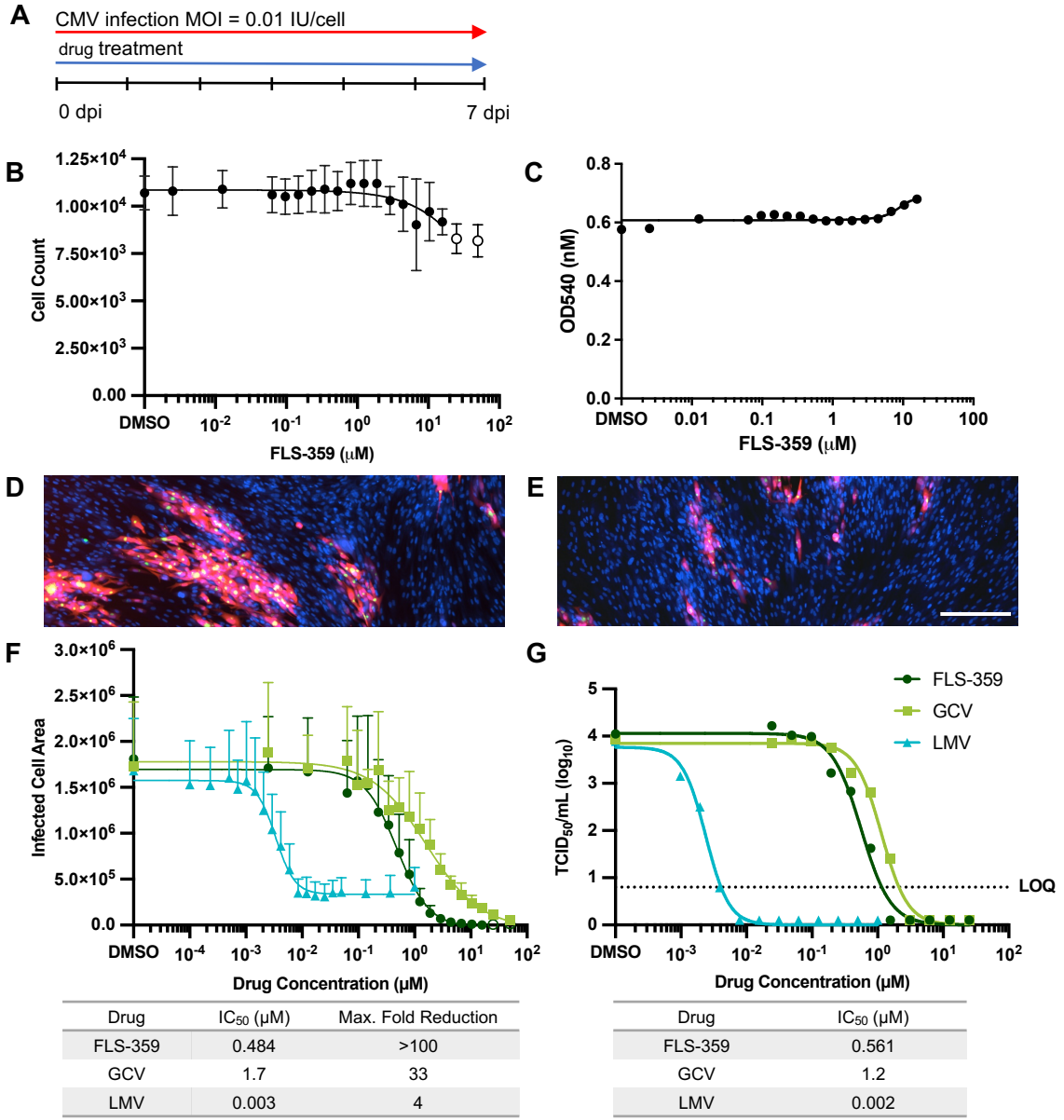

Drug	IC_{50} (μM)	Max. Fold Reduction
FLS-359	0.484	>100
GCV	1.7	33
LMV	0.003	4

Drug	IC_{50} (μM)
FLS-359	0.561
GCV	1.2
LMV	0.002

Figure 4. FLS-359 inhibits HCMV spread in fibroblasts. (**A**) Schematic representation of the spread assay. (**B-C**) Cytotoxicity was assessed in confluent MRC-5 cells after 7 days of FLS-359 treatment by DAPI staining for cell count (**B**) or neutral red uptake (**C**) (n=3). (**D-E**) Confocal images of MRC-5 cells infected with TB40/E-mCherry-UL99eGFP (0.01 IU/cell) at 7 dpi, treated with vehicle (**D**) or FLS-359 at 0.5 μM (**E**). Fluorescent mCherry (red) is expressed with immediate-early kinetics, eGFP (green) with late kinetics and DAPI (blue) locates nuclei. Scale bar is 300 μm. (**F**) Virus spread assay. CMV-infected cell area is quantified by mCherry fluorescence and plotted versus FLS-359, ganciclovir (GCV), or letermovir (LMV) concentrations; IC_{50} (mean +/- SD) and maximum reduction are reported (n=4) . (**G**) Virus yield assay. Cell-free virus at 7 dpi was quantified by $TCID_{50}$. LOQ; limit of quantification. IC_{50} is reported.

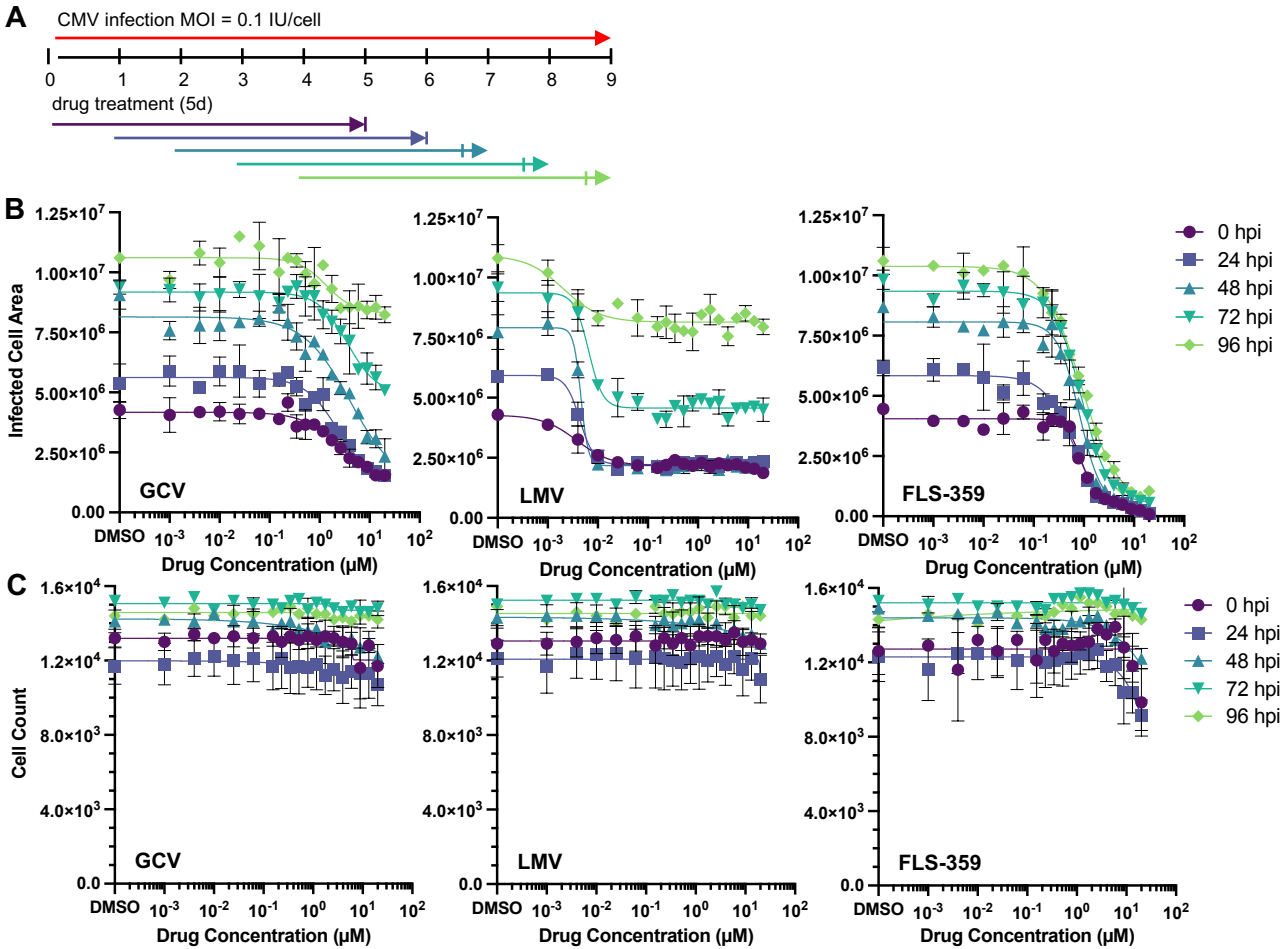

D

Time of Drug Addition	IC_{50} (μM)			Maximum Fold-Reduction		
(hpi)	GCV	LMV	FLS-359	GCV	LMV	FLS-359
0	2.5	0.004	0.9	3.2	2.0	11.6
24	2.3	0.004	0.6	4.5	2.7	33.4
48	4.1	0.005	0.8	7.5	3.7	21.2
72	3.6	0.007	0.9	1.9	2.0	17.6
96	1.4	0.002	0.9	1.3	1.3	21.8

Figure 5. FLS-359 is effective in a delayed treatment protocol. (**A**) Confluent MRC-5 cells were infected with TB40/E-mCherry-UL99eGFP (0.1 IU/cell). FLS-359, ganciclovir (GCV) or letermovir (LMV) was added at 0 hpi, or delayed for 24, 48, 72, or 96 h. After 5 days of drug treatment, infected cell area was quantified by mCherry fluorescence (**B**) and cell counts by nuclear DAPI stain (**C**). Mean +/- SD is shown (n=3). (**D**) Results in table format report IC_{50} and maximum fold-reduction.

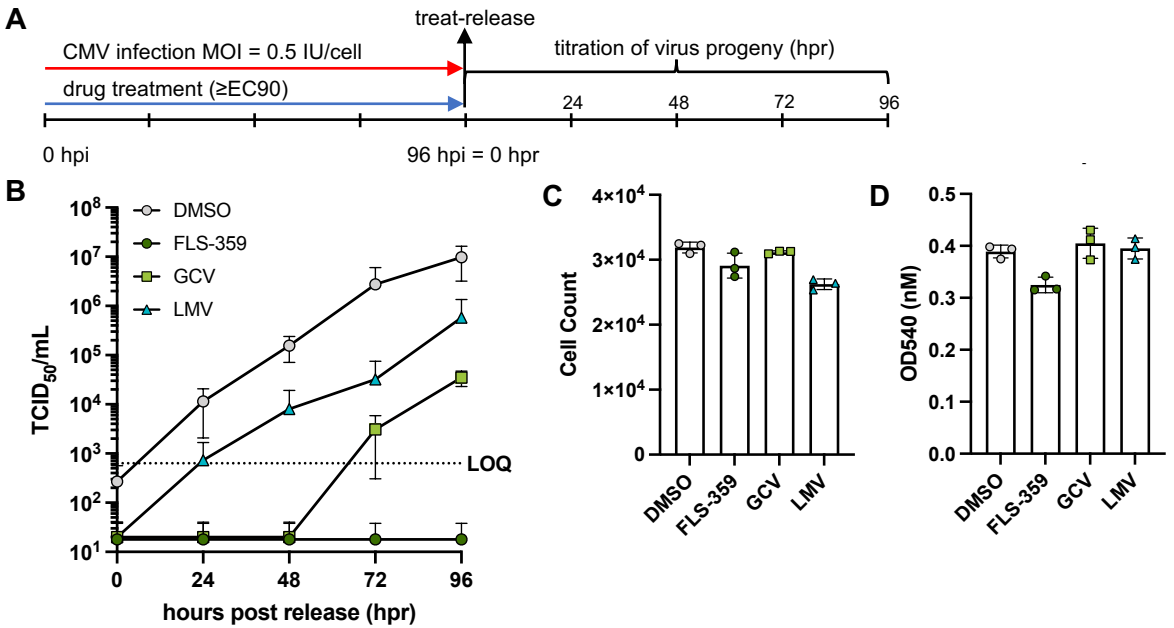

Figure 6. Long-term antiviral activity of FLS-359 following removal of drug. (**A**) Confluent MRC-5 cells were infected with TB40/E-mCherry-UL99eGFP (0.5 IU/cell) in the presence of drugs at their approximate EC90s (FLS-359, 5 µM; ganciclovir, GCV, 20 mM; letermovir, LMV, 0.05 µM). Infection proceeded for 96h, monolayers were washed 3x with buffer (PBS) and drug-free growth medium was added. Supernatant was sampled at 24h intervals over 4 days and virus was titered by $TCID_{50}$. (**B**) Cell-free virus titers as a function of time after release of the drug-induced block. LOQ, limit of quantification. (**C-D**) Cell viability was assessed at 96h after release of the drug block by cell count (**C**) or lactate dehydrogenase activity (**D**). Mean +/- SD is shown (n=3).

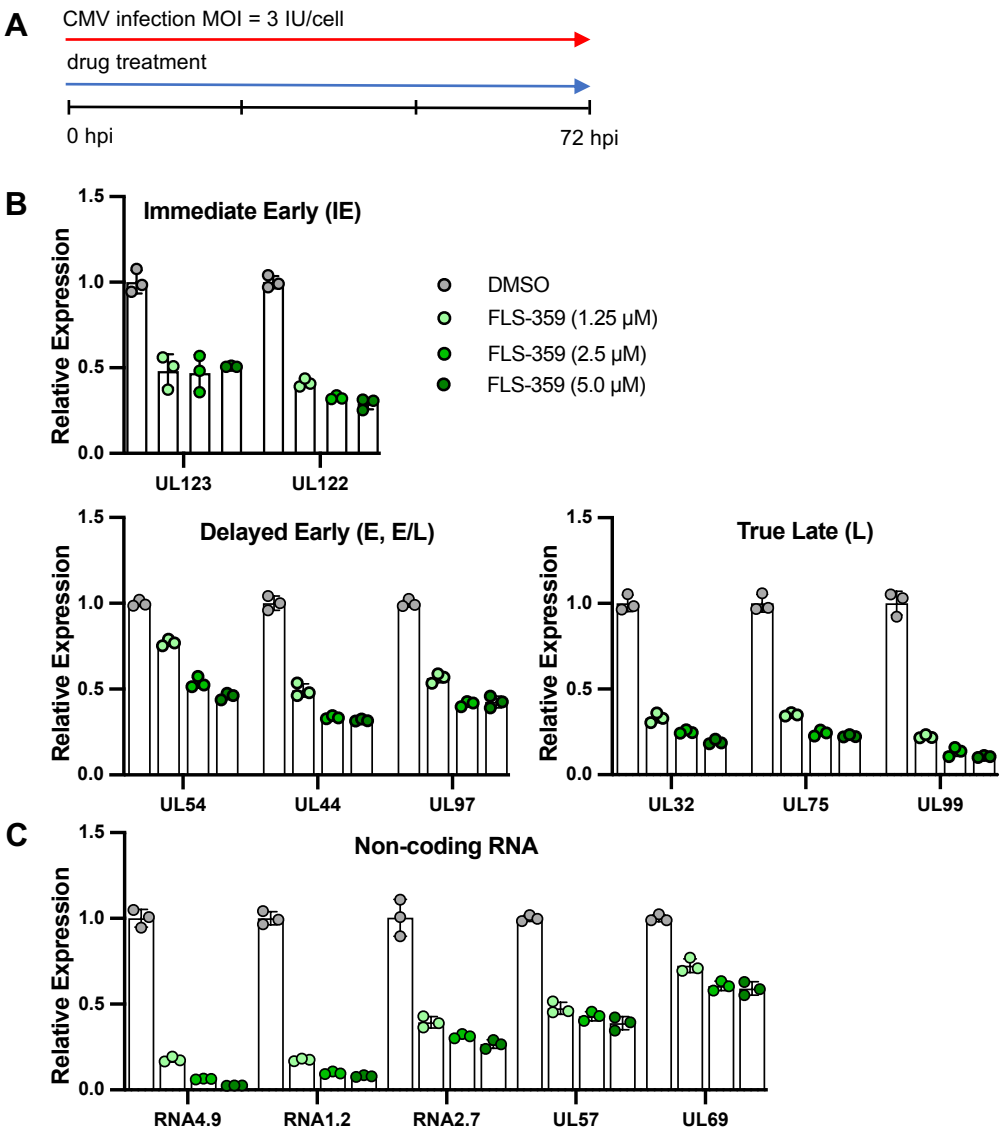

Figure 7. FLS-359 suppresses accumulation of all classes of viral RNAs. (**A**) MRC-5 cells were mock-infected or infected with TB40/E-mCherry-UL99eGFP (3 IU/cell). FLS-359 was added at indicated doses following adsorption, cell RNA was prepared at 72 hpi and viral RNAs were quantified relative to cellular GAPDH RNA by qRT-PCR. (**B**) Dot plots showing that FLS-359 reduces accumulation of all tested protein-coding RNAs, including multiple representatives of each kinetic class. (**C**) Dot plots showing FLS-359 reduces expression of multiple viral non-coding and protein-coding RNAs. Mean +/- SD is shown (n=3).

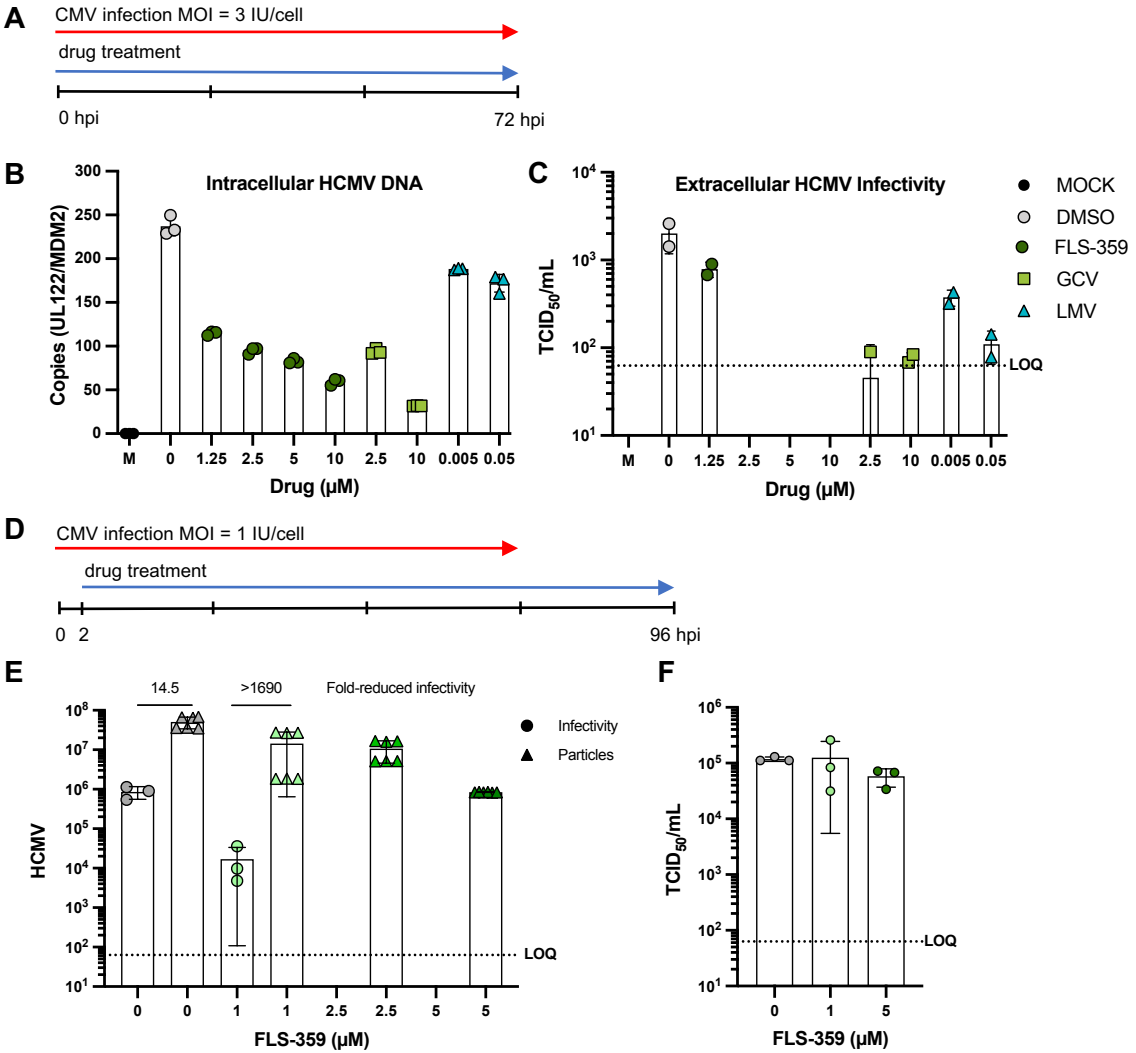

Figure 8. FLS-359 reduces intracellular HCMV DNA accumulation and extracellular virus production. (**A**) MRC-5 cells were mock-infected or infected with TB40/E-mCherry-UL99eGFP (3 IU/cell), treated with the indicated FLS-359, ganciclovir (GCV) and letermovir (LMV) doses and harvested at 72 hpi. (**B**) Cellular DNA was prepared, and HCMV DNA was quantified by qPCR using UL122-specific probes and normalized to cellular MDM2 DNA (n=3). (**C**) The effect of drugs on virus yield was monitored by $TCID_{50}$ assay (n=2). (**D**) MRC-5 cells were infected with TB40/E-mCherry-UL99eGFP (1 IU/cell) and treated with the indicated drug doses from 2 hpi to 96 hpi. (**E**) DNase I-resistant viral DNA was quantified by qPCR (n=6) and infectious virus was quantified by $TCID_{50}$ assay (n=3). (**F**) TB40/E-mCherry-UL99eGFP virus (10^5 IU/ml) was incubated with indicated drug doses for 24 h and infectious virus was quantified by $TCID_{50}$ assay (n=3). LOQ, limit of quantification; mean +/- SD is shown.

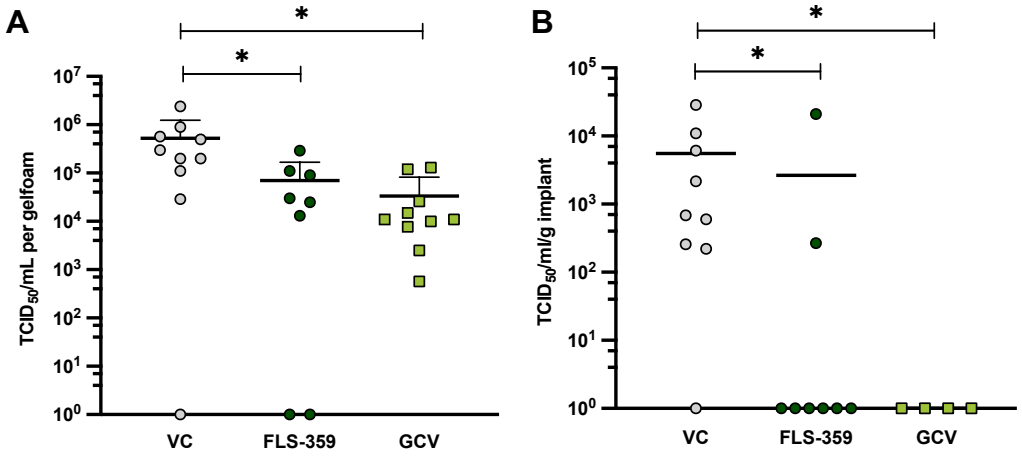

Figure 9. In vivo efficacy of FLS-359. (**A**) Gelfoam/human fibroblast model. MRC-5 cells were infected with TB40/E-mCherry-UL99eGFP (0.05 IU/cell), incubated for 24h, harvested, counted, and seeded ($1x10^6$ cells) into gelfoam plugs. After 3 days of incubation, plugs were implanted subcutaneously on the flanks of CIEA NOG mice. Beginning at 24h post-implantation, mice were treated with vehicle control (VC, 0.5% methyl cellulose + 0.5% Tween 80, p.o., b.i.d.), FLS-359 (50 mg/kg in VC, p.o., b.i.d.) or valganciclovir (GCV, 100 mg/kg in VC, p.o., b.i.d.). After 11 days of treatment, gelfoam plugs were harvested, and virus was quantified by $TCID_{50}$ assay. *, $p<0.03$. (**B**) Lung organoid model. Beginning at 2h prior to infection with TB40/E (4.25×10^5 IU) via direct injection into organoids, LoM were treated with vehicle control (VC, 0.5% methyl cellulose + 0.5% Tween80 in sterile distilled water; p.o., b.i.d.), FLS-359 (50 mg/kg in VC, p.o., b.i.d.), or ganciclovir (GCV, 100 mg/kg in VC, i.p., q.d.). After 17 days of treatment, implants were harvested and processed for $TCID_{50}$ determination. *, $p<0.04$. Variance was calculated by one-sided Kruskal-Wallis test followed by Dunn's multiple comparison test.

Table 1. FLS-359 exhibits broad-spectrum antiviral activity. Results are shown for representative assays (details in Methods). [1]SI, selectivity index; [2]SOC, standard of care and C, comparator compound; [3]HFF, human foreskin fibroblasts; [4]dNHBE, differentiated normal human bronchial epithelial cells; [5]PHH, primary human hepatocytes; [6]IC_{90}.

Virus/ Host Cell	Virus Family	FLS-359 IC_{50} (μM)	Host Cell CC_{50} (μM)	[1]SI CC_{50}/IC_{50}	[2]SOC/C IC_{50} (μM)	SOC/C
[3]SARS-CoV-2/ Human Calu3	β-Coronavirus	0.3	15.8	52.7	0.4	Remdesivir (C)
[3]Zika/ Human HFF	Flavivirus	0.4	41.6	104.0	2.8	Amodiaquine (C)
HCMV/ Human MRC5	β-Herpesvirus	0.5	>15.8	>40	2.7	Ganciclovir (SOC)
[4]Influenza A/ Human dNHBE	Orthomyxovirus	[6]1.2	>100	>83.3	[6]0.7	Ribavirin (C)
HCoV-OC43/ Human MRC5	β-Coronavirus	1.7	>50	>30.1	0.1	Remdesivir (C)
[3]Junin/ Human HFF	Arenavirus	3.2	>25	>7.8	0.2	RIID E-1 (C)
[5]Hepatitis B/ Human PHH	Hepadnavirus	4.8	>10	>2.1	0.03	Tenofovir (SOC)
Epstein-Barr/ Human Akata	γ-Herpesvirus	3.8	>100	>26.3	43	Ganciclovir (C)
RSV/ Human MRC5	Ortho-pneumovirus	6.7	>12.5	>1.9	16.1	Ribavirin (SOC)

Table 2. Multiple SIRT2 inhibitors reduce HCMV spread. Non-linear regression analysis was used to calculate absolute IC_{50}s from infected MRC-5 cell area measured at 7 dpi (n=2). CC_{50}s for uninfected MRC-5 cells were determined by DAPI cell count after a 7-day treatment. Underlying data is in Supplemental Figure 3. [1]SI, Selectivity Index; [2]Reported literature values (cited in text), except FLS-359, which from Figure 4; [3]Infected cell area did not reach 0 at the highest drug concentration tested.

Compound	HCMV IC_{50} (μM)	MRC5 CC_{50} (μM)	[1]SI CC_{50}/IC_{50}	[2]SIRT2 IC_{50} (μM)	Structure
FLS-359	0.5	>15.8	>31.6	3.0	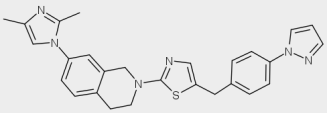
AGK2	[3]3.4	>100	>29.4	3.5	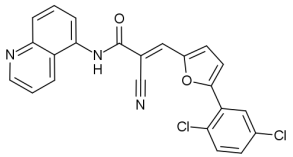
AK-7	8.2	>25	>3	15.5	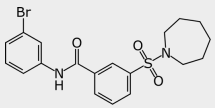
MIND4	14.4	19.8	1.4	3.5	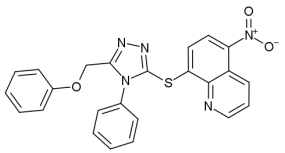
SirReal2	[3]14.9	>20	>1.3	0.14 - 0.44	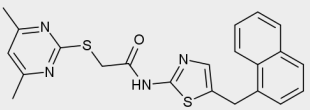
TM	26.0	46.3	1.8	0.028	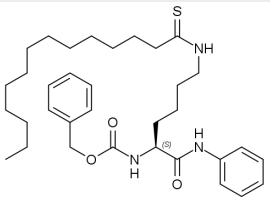

Supplemental Material

An allosteric inhibitor of sirtuin 2 deacetylase activity exhibits broad-spectrum antiviral activity

Kathryn L. Roche,[1] Stacy Remiszewski,[1] Matthew J. Todd,[1] John L. Kulp III,[1] Liudi Tang,[1] Alison V. Welsh[1], Ashley P. Barry,[2] Chandrav De,[3] William W. Reiley,[4] Angela Wahl,[3] J. Victor Garcia-Martinez,[3] Micah A. Luftig,[2] Thomas Shenk,[1,5] James R. Tonra,[1] Eain A. Murphy,[1,6] and Lillian W. Chiang,[1]

Corresponding author: Lillian W. Chiang, lillian@evrysbio.com

This file includes:

Supplemental Figures 1-8 with accompanying legends

Supplemental Tables 1-3 with accompanying legends

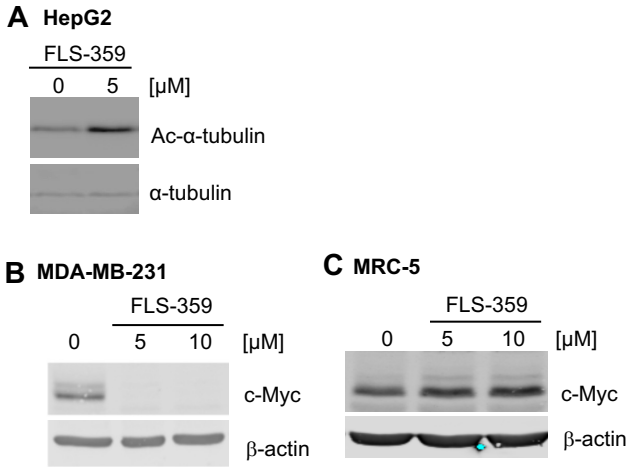

Supplemental Figure 1. FLS-359 is active in cultured cells. (**A**) HepG2 cells were treated with FLS-359 plus 1 μM trichostatin A (TSA) for 24 h and levels of acetylated α-tubulin (Ac-α-tubulin) were determined by western blot. Total α-tubulin was monitored as a control. (**B**) MDA-MB-231 cells or (**C**) MRC-5 fibroblasts were treated with drug for 72h and c-Myc was monitored by western blot with β-actin as a control. Western blots are representative of three independent experiments.

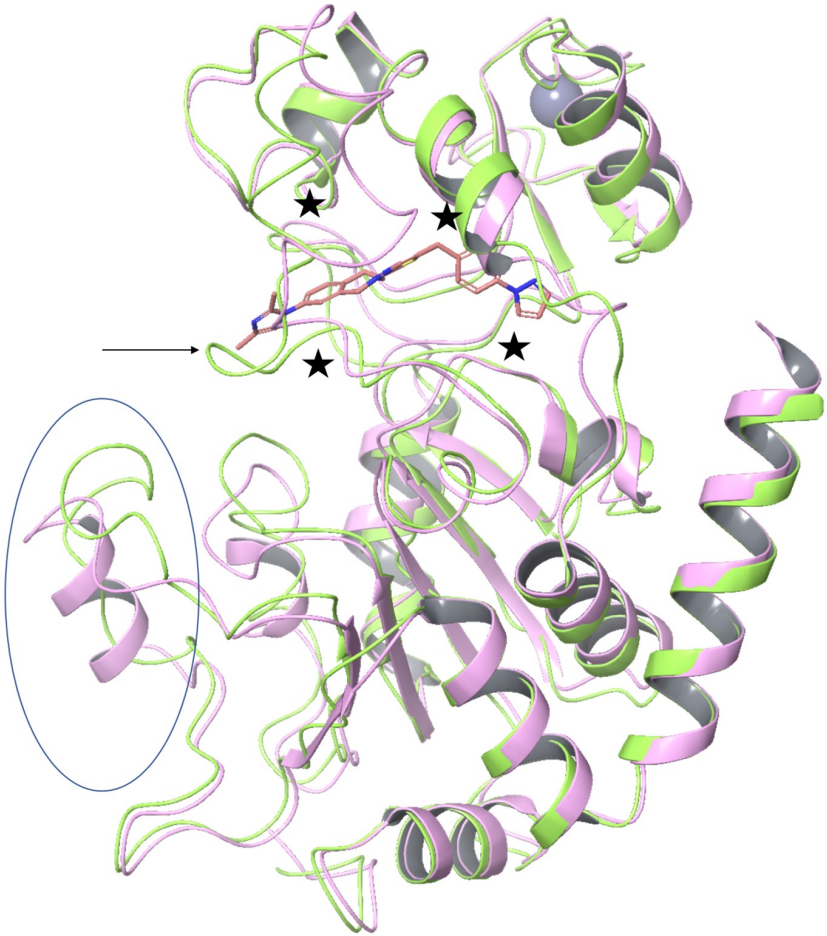

Supplemental Figure 2. Shifts of SIRT2 apo structure upon FLS-359 binding. The oval highlights residues that are in an alpha helix confirmation in the apo structure (purple ribbons, PDB ID 3ZGO) but shift to an unstructured loop with FLS-359 binding (green ribbons). The arrow identifies a shift in a loop over the drug binding site, between the apo and FLS-359-bound SIRT2 structures. Stars mark the domain (center of the clamshell) that opens when FLS-359 is bound.

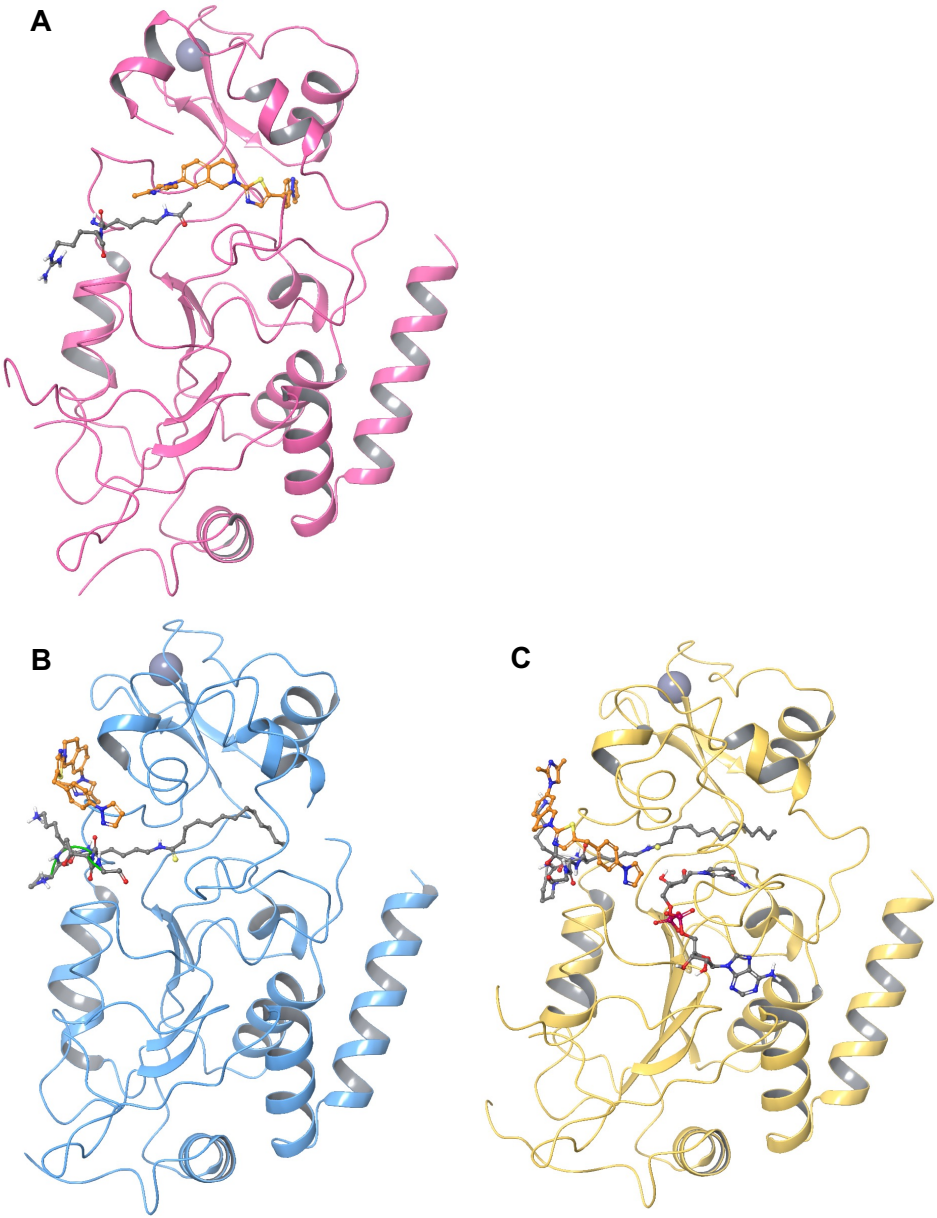

Supplemental Figure 3. Docking analysis predicts that a myristoylated peptide competes with FLS-359 for binding to SIRT2. The interaction of FLS-359 with known SIRT2-acyl peptide structures was analyzed by flexible protein docking using Glide, a module of the Schrödinger software. (**A**) Acetyated peptide (TGGK^{Ac}APR; gray carbon atoms) bound to SIRT2 (PDB ID 4RMI) does not block FLS-359 (orange carbon atoms) binding in the extended C site. (**B**) Thiomyristoylated peptide (PKK^{TMy}TG; gray carbon atoms) bound to SIRT2 (PDB ID 4R8M) displaces FLS-359 to the protein surface. (**C**) Thiomyristoylated peptide plus NAD (blue carbon atoms) bound to SIRT2 (PDB ID 4X3P) displaces FLS-359.

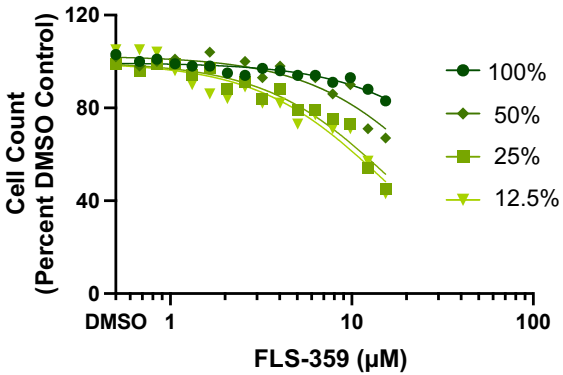

Supplemental Figure 4. FLS-359 does not significantly inhibit the growth of MRC-5 fibroblasts at the IC_{90} for inhibition of HCMV. Cells were plated to achieve the indicated initial levels of confluence, treated with FLS-359 1h later, and counted after 6 days. FLS-359 IC_{50} (0.5 μM) and IC_{90} (2.06 μM) were determined on confluent cells.

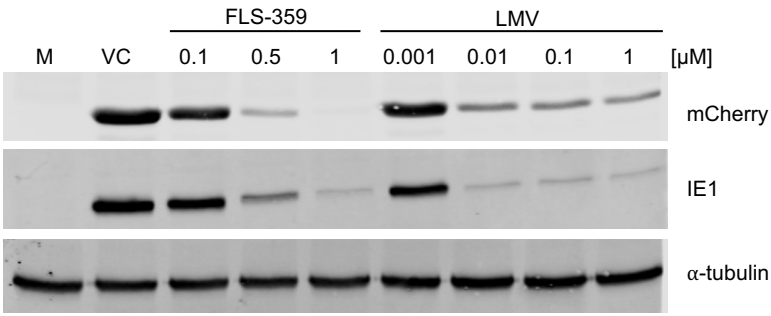

Supplemental Figure 5: FLS-359 and letermovir reduce the accumulation of an HCMV immediate-early protein. MRC-5 cells were mock-infected or infected with TB40/E mCherry UL99-eGFP (0.01 IU/cell) and treated with FLS-359 or letermovir (LMV). Cell lysates were harvested at 7 dpi, and mCherry, IE1, and alpha-tubulin were detected by western blot; M, mock-infected; VC, vehicle control. This image is representative of two independent experiments.

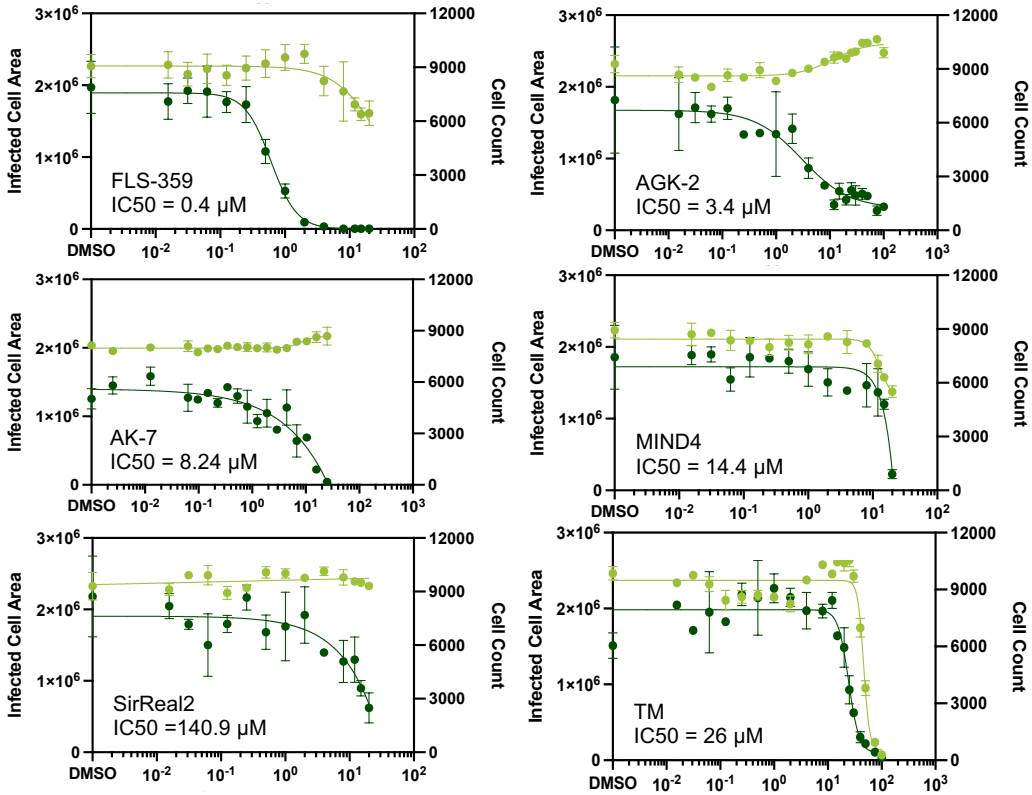

Supplemental Figure 6. Multiple SIRT2 inhibitors block HCMV growth. Confluent MRC-5 cells were infected with TB40/E-mCherry-UL99eGFP (0.01 IU/cell). Drug or vehicle (DMSO) was added after inoculation and the fluorescent area marking infected cells was quantified at 7 dpi (dark green circles). Cell viability was monitored by staining drug-treated (7 days), uninfected MRC-5 cells with DAPI and quantifying nuclei (light green circles). Mean +/- SD is shown (n=3).

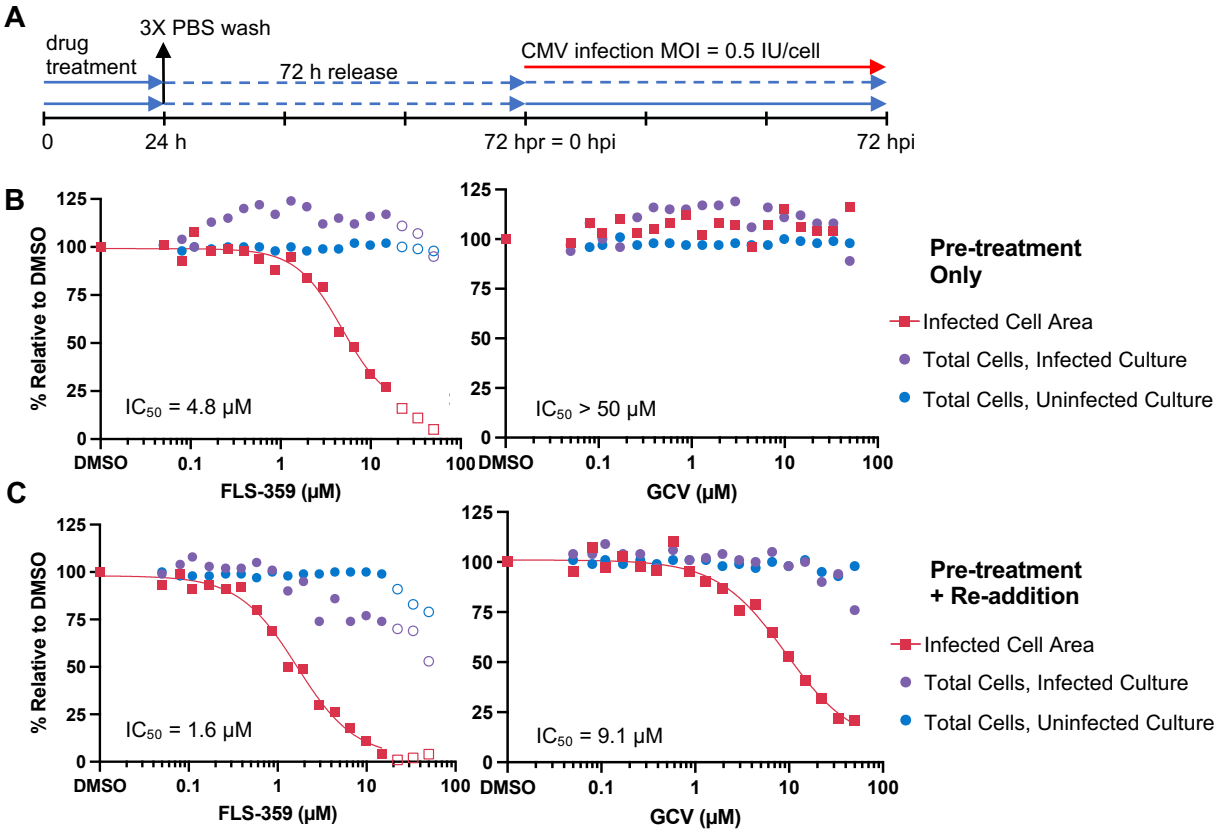

Supplemental Figure 7. Pre-treatment of uninfected cells with FLS-359 followed by a drug-free period protects against subsequent HCMV infection. (**A**) MRC-5 cells were pre-treated with FLS-359 (5 µM) or GCV (20 µM) for 24h followed by a 72h drug-free period. Then they were infected with TB40/E-mCherry-UL99eGFP (0.5 IU/cell) in the absence of drug or with drug re-added. Uninfected cells, drug-treated in the same manner, served as a control. (**B-C**) Infected cell area was quantified by mCherry fluorescence and cell counts by nuclear DAPI stain at 72 hpi. Results are representative of three independent experiments.

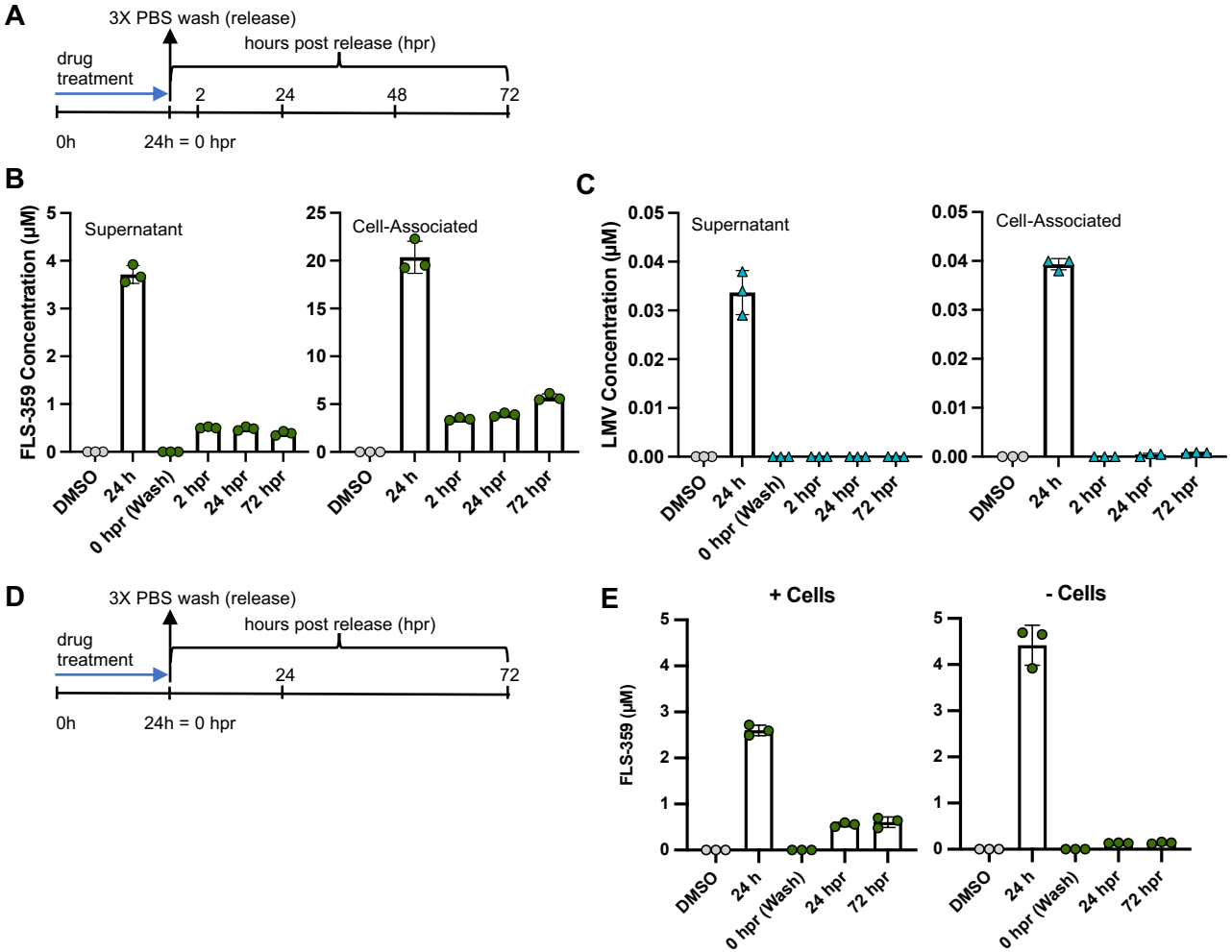

Supplemental Figure 8. FLS-359 exhibits a long half life within MRC-5 cells. (**A**) Uninfected cells were treated with drug (FLS-359 = 5 µM; LMV = 0.05 µM). After 24h, supernatant was collected, monolayers were washed 3x to remove drug and cells were replenished with drug-free media. Supernatants and cells were then assayed for residual drug levels at 2, 24 or 72h post-release. (**B-C**) Supernatant and cell-associated drug concentrations were determined by mass spectrometry. **(D)** Medium containing 5 µM FLS-359 was added to plastic tissue culture dishes with or without a confluent monolayer of MRC5 cells. Sampling of the supernatant was conducted after a 24h incubation at 37°C, followed by 3X washes with PBS, collection of the final wash, and replenishment of drug-free medium to the dishes. Supernatant samples were then collected at 24 and 72h post drug-removal. (**E**) FLS-359 drug concentrations as determined by mass spectrometry. Mean +/- SD is shown (n=3).

Supplemental Table 1. FLS-359-SIRT2 Data Collection and Refinement Statistics. Numbers in parentheses refer to the highest resolution bin.

	Parameter	Value
Data Collection Statistics	Crystal identifier	xctc3-fls-03-08
	Inhibitor	FLS-359
	Space Group	$P2_1$
	Unit cell parameters (Å, °)	a=36.8, b=56.0, c=139.6, α=90.0, β=94.5, γ=90.0
	Resolution (Å)	139.15-1.75 (1.78-1.75)
	# Unique reflections	56312 (3005)
	I/σ/I	9.5 (1.9)
	Completeness (%)	98.6 (98.9)
	Multiplicity	3.5 (3.4)
	R_{meas}	0.09 (0.73)
	R_{pim}	0.05 (0.39)
	CC(1/2)	0.996 (0.664)
Refinement Statistics	Resolution (Å)	139.15-1.75 (1.78-1.75)
	R_{work}	0.159 (0.236)
	R_{free}	0.210 (0.284)
	Completeness (%)	98.3 (98.6)
	r.m.s.d. bonds (Å)	0.009
	r.m.s.d. angles (°)	1.56

Supplemental Table 2. To evaluate FLS-359 pharmacokinetics, a single dose of FLS-359 was administered (p.o.) to female Balb/c mice as a suspension in 0.5% methylcellulose/0.5% Tween80/water. Plasma samples from groups of three animals were assayed over the course of 24h. Mean +/- SD is presented.

Dose (mg/kg)	50
C_{max} (μM)	89.3 ± 11
T_{max} (h)	2.0 ± 0
$T_{1/2}$ (h)	5.8 ± 1.4
$AUC_{0-\infty}$ (μM·h/mL)	713.0 ± 33
$AUC_{0-\infty}$ /1 mg dose	14.3 ± 1.0

Supplemental Table 3. Primers used in quantitative PCR assays.

Transcript	Forward (5'-3')	Reverse (5'-3')
SetDB1	GACTACAATACCGGGACAGTAGC	CCCAGCATCACCTGAATCAAT
BZLF1	AGCCTGCTCCTGAGAATGCT	CCACTGCTGCTGCTGTTTGA
BMRF1	CGTGCCAATCTTGAGGTTTT	CGGAGGCGTGGTTAAATAAA
BLLF1	CCCGCTGGACTTTTACGA	GCATGGAGAGGTTTGAGA
UL123	GCCTTCCCTAAGACCACCAAT	ATTTTCTGGGCATAAGCCATAATC
UL122	ATGGTTTTGCAGGCTTTGATG	ACCTGCCCTTCACGATTCC
UL99	GCTGCGGCTCTGCGGTAG	GCGAAACGTCGAGCGCAC
UL97	CGGCGTCACCACTTTGACC	CGTCACGCATCACGTCACTT
UL75	TCTCCGTCGTATGCACCAGC	GATCGCCGACTTTGCCCTAC
UL69	GCAGTGCCACGAGTGTCA	GGTGAGATCCAATAGCGACTGCT
UL57	TGAACGCAGAAACGCAGGAG	GAAATCCGCCTCCACCGTGA
UL54	CCCTCGGCTTCTCACAACAAT	GGCGAGTTAGTCTTGGCCAT
UL44	TACAACAGCGTGTCGTGCTCCG	CATGCGTATCAACGTGCAGCTG
UL32	GGTTTCTGGCTCGTGGATGTCG	CACACAACACCGTCGTCCGATTAC
RNA 4.9	GTAAGACGGGCAAATACGGT	AGAGAACGATGGAGGACGAC
RNA 2.7	TCCATGTTTCCATCCTTTCA	AATCAGCGTTGCAGTAGTCG
RNA 1.2	TGACAACGCCTTGTATAGCC	AGACTGTCGTGGTCGATGAA
GAPDH	ACCCACTCCTCCACCTTTGAC	CTGTTGCTGTAGCCAAATTCGT
MDM2	CCCCTTCCATCACATTGCA	AGTTTGGCTTTCTCAGAGATTTCC